BNL-229898-2026-TECH

CA/AP/752

An absolute recoil-carbon polarimeter for polarized light-ions at the BNL Booster

V. Shmakova

July 2026

Collider Accelerator Department

Brookhaven National Laboratory

U.S. Department of Energy

USDOE Office of Science (SC), Nuclear Physics (NP)

DISCLAIMER

An absolute recoil-carbon polarimeter for polarized light-ions at the BNL Booster

V. Shmakova[1], E. Shulga[1], X. Chu[1], J. Datta[2], K. O. Eyser[1], K. Hernandez[1], K. Hock[1], H. Huang[1], G. Mahler[1], P. MohanMurthy[3], R. Porqueddu[1], D. Raparia[1], V. Schoefer[1], P. Shanmuganathan[1], N. Wuerfel[3], Z. Zhang[1], and F. Rathmann[1]

[1]Brookhaven National Laboratory, Upton, New York 11973, USA
[2]Center for Frontiers in Nuclear Science, Physics and Astronomy Department, Stony Brook University, Stony Brook, New York 11794, USA
[3]Laboratory for Nuclear Science, Massachusetts Institute of Technology, 77 Mass. Ave., Cambridge, MA 02139, USA

June 25, 2026

Contents

Abstract

We describe a recoil-carbon polarimeter for the BNL Booster synchrotron capable of measuring the transverse polarization of both the polarized proton beam and the polarized ^{3}He ion beam throughout the acceleration cycle. The instrument addresses a critical gap in the BNL polarized beam program: no independent polarization measurement currently exists in the injector chain between the 200 MeV Linac polarimeter and the AGS. The proposed new polarimeter will provide continuous, absolute polarization measurements at the Booster stage, supplying additional anchor points for the polarization transmission through the accelerator chain. The polarimeter

is based on elastic pC and ^{3}He C scattering from a thin internal carbon target, with detection of the recoil ^{12}C nucleus in a fixed six-station silicon detector ring. A single detector geometry provides continuous kinematic coverage from injection to extraction for both beam species without mechanical adjustment. For pC scattering, the available data and the Bonin parametrization provide a well-established basis for estimating the analyzing power and figure of merit over the Booster energy range; for ^{3}He C the sole experimental anchor is a measurement at 443 MeV, and the Booster polarimeter itself is identified as the instrument to map the analyzing power across the remainder of the acceleration ramp by a ramp-and-return calibration that anchors the absolute ^{3}He polarization scale to a few percent. Provision for future deuteron polarimetry is incorporated in the chamber design without modification to the existing geometry. With appropriate detector upgrades, the same recoil-carbon technique can be extended to deuteron beams, for which analyzing power data are already available, and, with future analyzing-power measurements, also to ^{6}Li and ^{7}Li beams, making the polarimeter a versatile instrument for the full range of light polarized ion species anticipated at BNL.

1 Introduction

The BNL polarized beam program requires high polarization at the Electron Ion Collider (EIC), placing stringent demands on polarization transmission through every stage of the injector chain. RHIC completed its final run in February 2026, after which the complex transitions to EIC construction while the Alternating Gradient Synchrotron (AGS), in continuous operation since 1960, undergoes a multi-year refurbishment including extensive recabling and hardware upgrades. During this interval, and again once EIC operations commence, a polarimeter at the Booster stage will provide absolute anchor points for polarization transmission. Currently, no independent polarization measurement exists in the injector chain between the 200 MeV Linac polarimeter for protons, the ^{3}He polarimeter at EBIS (Electron Beam Ion Source), and the AGS. Polarimetry in the BNL Booster is required to monitor and optimize the polarization of both the polarized proton beam and the polarized ^{3}He ion beam during acceleration from injection to extraction. The Booster accelerates the proton beam from the Linac injection energy to its maximum extraction energy [1], and accelerates the polarized ^{3}He ion beam delivered by the EBIS [2] at $T_{\rm inj}^{^3\rm He} = 2\,\rm MeV/u$ toward extraction. The two species are not extracted at the same rigidity: for protons the extraction spin tune is $G\gamma = 4.659$ at $T_p = 1500\,\rm MeV$ ($B\rho = 7.51\,\rm T\,m$), while for helions the relevant working points are $G\gamma = 7.5$ at $T_{^3\rm He} = 2226\,\rm MeV$ ($742\,\rm MeV/u$, $B\rho = 6.97\,\rm T\,m$) or $G\gamma = 10.5$ at $T_{^3\rm He} = 4239\,\rm MeV$ ($1413\,\rm MeV/u$, $B\rho = 10.78\,\rm T\,m$). For the purpose of this analysis both beams are evaluated at the common reference rigidity $B\rho \approx 7.5\,\rm T\,m$ listed in Table 1. The Booster maximum rigidity is approximately $17.5\,\rm T\,m$; the practical extraction limit is constrained by the AGS injection and extraction hardware to approximately $9.5\,\rm T\,m$.

For a given magnetic rigidity in the Booster, the relation between proton-beam and ^{3}He-ion energies follows from the equality of magnetic rigidity,

$$B\rho = \frac{p}{q}. \tag{1}$$

The corresponding beam parameters, including injection and extraction kinetic energies, momentum, Lorentz factors, velocity factors, and spin tunes, are summarized in Table 1.

The polarimeter concept considered here is based on scattering from a carbon target. Recoil-carbon polarimetry has a long history at intermediate energies, from foundational measurements and parametrizations of the pC analyzing power [3,4] to broader programs at storage rings such as the Indiana Cooler and COSY [5,6]. The reactions employed here are

$$p + {}^{12}\rm C \to p + {}^{12}C, \tag{2}$$

$${}^3\rm He + {}^{12}C \to {}^3He + {}^{12}C, \tag{3}$$

with detection of the recoil ^{12}C nuclei. The recoil carbon nuclei emerge predominantly at laboratory angles near 90°, with kinetic energies determined uniquely by two-body kinematics. This provides a clean method for identifying elastic events independent of beam energy.

This polarimeter operates in a regime fundamentally different from the Coulomb-Nuclear Interference (CNI) polarimeters used at the AGS and RHIC. The CNI analyzing power formalism [7] is valid only in the Regge regime of hadronic scattering, where the forward elastic amplitude is dominated by Pomeron exchange and varies smoothly and slowly with energy, and the total cross section and the real-to-imaginary ratio ρ of the hadronic amplitude are well-defined slowly-varying quantities. This smooth behavior sets in above $p_{\mathrm{lab}} \sim 1\,\mathrm{GeV/c}$ to $2\,\mathrm{GeV/c}$; below this threshold the amplitude is dominated by individual baryon and meson resonances, the total cross section varies rapidly with energy, and the CNI parametrization is no longer applicable. At Booster energies ($p \sim 0.6\,\mathrm{GeV/c}$ to $2.3\,\mathrm{GeV/c}$ for protons) nuclear elastic scattering with a measured analyzing power is therefore the correct approach, and the Booster polarimeter and the AGS pC CNI polarimeter [8, 9] are complementary by necessity, covering energy regimes where fundamentally different reaction mechanisms are at work.

A key requirement for Booster operation is that the detector geometry must provide continuous coverage over the full energy range of both beams listed in Table 1, without mechanical adjustment during the acceleration cycle. Because the recoil-carbon kinematics scale smoothly with beam momentum, a fixed detector configuration can satisfy this requirement, as discussed in detail in Sec. 2.

For the proton beam, elastic pC analyzing-power and differential-cross-section data exist over a wide energy range and provide an established basis for polarimetry, see, e.g., Refs. [3–6]. For the ^{3}He ion beam, elastic ^{3}He C data [10], including measurements of analyzing power and differential cross section at 443 MeV in the lower part of the Booster energy range, provide the experimental anchor point for extending recoil-carbon polarimetry to polarized ^{3}He beams.

The following sections develop the elastic scattering kinematics for pC, ^{3}He C, dC, and ^{6,7}Li C scattering using the beam parameters given in Table 1, and define a detector configuration capable of providing polarimetry for both beams throughout the Booster acceleration cycle.

2 Elastic scattering kinematics

The polarimeter concept is based on elastic scattering of the circulating beam particles from a carbon target and detection of the recoil ^{12}C nuclei. The relevant reactions are pC and ^{3}HeC elastic scattering. Because elastic scattering is a two-body process, the recoil energy and recoil angle are uniquely determined by the beam energy and the masses of the projectile and target. This allows clean identification of elastic events over the full Booster energy range listed in Table 1.

We consider elastic scattering of a projectile of mass m and kinetic energy T from a target of mass M initially at rest. The projectile total energy is

$$E = T + m. \tag{4}$$

The projectile momentum is

$$p = \sqrt{E^2 - m^2}. \tag{5}$$

The invariant mass squared of the system is

$$s = m^2 + M^2 + 2ME. \tag{6}$$

The exact laboratory-frame kinematics are obtained from four-momentum conservation and the on-shell condition for the recoil nucleus, using standard relativistic reaction-kinematics conventions

Table 1: BNL Booster parameters for the polarized proton beam and polarized ^{3}He^{++} ion beam. The proton beam is injected from the 200 MeV Linac at $T^p_{\rm inj} = 200\,$MeV and the ^{3}He^{++} ion beam is injected from EBIS at $T^{^3\rm He}_{\rm inj} = 2\,$MeV/u. Both beams are evaluated at a common reference rigidity $B\rho \approx 7.51\,$T m, corresponding to $T^p_{\rm extr} = 1500\,$MeV ($G\gamma = 4.659$) for protons and $T^{^3\rm He}_{\rm extr} = 2496\,$MeV ($832\,$MeV/u, $G\gamma = -7.917$) for ^{3}He^{++}. The actual extraction rigidity of each species is determined by its spin-resonance structure and need not coincide with this reference value. The Booster maximum rigidity is $\approx 17.5\,$T m; extraction to the AGS is limited by the injection and extraction hardware to $\approx 9.5\,$T m. The difference in repetition frequency reflects the lower pulse rate of the EBIS source compared to the Linac. Rest masses and anomalous magnetic moments are taken from CODATA 2018 [11].

Quantity	Symbol	Unit	Proton beam	^{3}He^{++} beam
Rest mass	m	MeV/c^2	938.272	2808.391
Charge state	q	e	+1	+2
Anomalous magnetic moment	G	–	+1.792847	−4.1914
Injection kinetic energy	$T_{\rm inj}$	MeV (MeV/u)	200	6 (2)
Extraction kinetic energy	$T_{\rm extr}$	MeV (MeV/u)	1500	2496 (832)
Injection momentum	$p_{\rm inj}$	MeV/c	644	184
Extraction momentum	$p_{\rm extr}$	MeV/c	2251	4500
Injection magnetic rigidity	$B\rho_{\rm inj}$	T·m	2.150	0.306
Extraction magnetic rigidity	$B\rho_{\rm extr}$	T·m	7.506	
Injection Lorentz factor	$\gamma_{\rm inj}$	–	1.213	1.002
Extraction Lorentz factor	$\gamma_{\rm extr}$	–	2.599	1.889
Injection velocity factor	$\beta_{\rm inj}$	–	0.566	0.065
Extraction velocity factor	$\beta_{\rm extr}$	–	0.923	0.848
Injection revolution frequency	$f_{\rm rev,inj}$	MHz	0.841	0.097
Extraction revolution frequency	$f_{\rm rev,extr}$	MHz	1.371	1.260
Injection spin tune	$\nu_{s,\rm inj} = G\gamma_{\rm inj}$	–	+2.175	−4.200
Extraction spin tune	$\nu_{s,\rm extr} = G\gamma_{\rm extr}$	–	+4.659	−7.917
Repetition frequency	$f_{\rm rep}$	Hz	7.5	1.0
Repetition period	$T_{\rm rep} = 1/f_{\rm rep}$	ms	133	1000
Acceleration ramp time	$T_{\rm ramp}$	ms	≈ 75	≈ 75
Bunches per cycle	n_b	–	1	1[a]
Intensity per bunch	N_b	10^{11}	3.4	1.0 (2.5 design)
Intensity per cycle	$N_{\rm cyc} = n_b\,N_b$	10^{11}	3.4	1.0 (2.5 design)

[a]The ^{3}He beam is injected as 4 bunches and merged into a single bunch during a momentum-hold (flat porch) at $G\gamma = -4.5$ ($T_{^3\rm He} \approx 212\,$MeV, $B\rho \approx 1.85\,$T m). This merging scheme was demonstrated with unpolarized helions.

as in Ref. [12]. The scattered projectile momentum as a function of the forward laboratory angle θ is

$$p'(\theta) = \frac{p\left[(EM + m^2)\cos\theta + (E+M)\sqrt{M^2 - m^2\sin^2\theta}\right]}{(E+M)^2 - p^2\cos^2\theta}. \tag{7}$$

The recoil-carbon kinetic energy is then

$$T_C(\theta) = \frac{p^2\left[M + E\sin^2\theta - \cos\theta\sqrt{M^2 - m^2\sin^2\theta}\right]}{(E+M)^2 - p^2\cos^2\theta}. \tag{8}$$

The recoil-carbon laboratory angle is related to the forward projectile angle by

$$\tan\theta_C(\theta) = \frac{p'(\theta)\sin\theta}{p - p'(\theta)\cos\theta}. \tag{9}$$

Equations (7)–(9) define the exact elastic locus in the laboratory frame and form the basis for all kinematic correlations used in the following sections.

2.1 Fixed-geometry carbon recoil detection for p, d, ^{3}He, ^{6}Li, and ^{7}Li beams

Figure 1 shows the recoil ^{12}C laboratory angle θ_C as a function of the forward beam laboratory angle for elastic scattering of the five light-ion polarized beam species expected at BNL, protons, ^{3}He, and those potentially coming in the future, deuterons, ^{6}Li, and ^{7}Li, on a carbon target. Results are shown at three magnetic rigidities $B\rho = 1.5$, 5.0, and 7.5 T m spanning the Booster acceleration range. The non-relativistic billiard limit $\theta_C = 90^\circ - \theta/2$, which follows from momentum conservation in the limit of a light projectile scattering from a much heavier target, is included for reference. In all cases the recoil carbon nuclei emerge predominantly near $\theta_C = 70^\circ$–90° for forward beam angles up to $\sim 30^\circ$, and the dependence on beam energy across the Booster ramp is weak. This demonstrates that a single fixed recoil-ring detector geometry centred near 90° provides kinematic acceptance for all species throughout the acceleration cycle. The forward beam angle range relevant for the coincidence detector ($\theta \lesssim 15^\circ$) lies well within the region of stable recoil acceptance for all species.

2.2 Recoil energy, detector requirements for pC and ^{3}HeC elastic scattering

Because the carbon mass is much larger than the proton mass and still significantly larger than the ^{3}He mass, the recoil carbon nuclei emerge predominantly at large laboratory angles. Over the full Booster energy range given in Table 1, the recoil carbon angles remain concentrated near

$$\theta_C \approx 70^\circ \text{ to } 90^\circ. \tag{10}$$

This is a key feature enabling a fixed recoil detector geometry.

The recoil kinetic energy is obtained exactly from Eq. (8). At fixed beam energy it increases as the forward projectile angle increases, or equivalently as the recoil angle decreases away from 90°.

For the proton beam, the recoil carbon kinetic energies range from the sub-MeV region near injection to several tens of MeV near extraction. For the ^{3}He ion beam, the recoil energies are correspondingly larger due to the larger projectile mass and momentum at the same magnetic rigidity.

The forward scattered projectile emerges at relatively small laboratory angles. The relation between forward scattering angle and beam momentum follows directly from the exact two-body kinematics discussed above and is illustrated for the relevant beam species and energies in Figs. 1 and 2.

These kinematic properties form the basis of the polarimeter design. The correlation between recoil carbon laboratory angle θ_C and projectile laboratory angle θ is shown in Fig. 2 for pC and ^{3}HeC elastic scattering at Booster injection and extraction energies. As seen in the figure, over the full Booster energy range and for projectile scattering angles up to about 30°, the recoil carbon nuclei are confined to a relatively narrow angular interval near 70° to 90°, with only a weak dependence on beam species and beam energy. This allows the recoil carbon nuclei to be detected in silicon detectors placed at fixed laboratory angles near 90° throughout the Booster acceleration cycle. Optional forward detectors placed at small laboratory angles can be used to detect the scattered proton or ^{3}He ion beam particles in coincidence. The unique correlation between recoil angle and recoil energy ensures clean identification of elastic events and separation from inelastic background over the full Booster energy range.

The recoil carbon kinetic energy as a function of recoil laboratory angle θ_C for pC and ^{3}HeC elastic scattering over the full Booster energy range is shown in Fig. 3. In contrast to the weak dependence of recoil angle on beam energy seen in Fig. 2, the recoil kinetic energy exhibits a strong dependence on both beam species and recoil angle. For both beams, the recoil energy increases as θ_C decreases from 90° toward smaller angles. For the proton beam, the recoil energies remain below approximately 80 MeV even at extraction, while for the ^{3}He ion beam the recoil energies

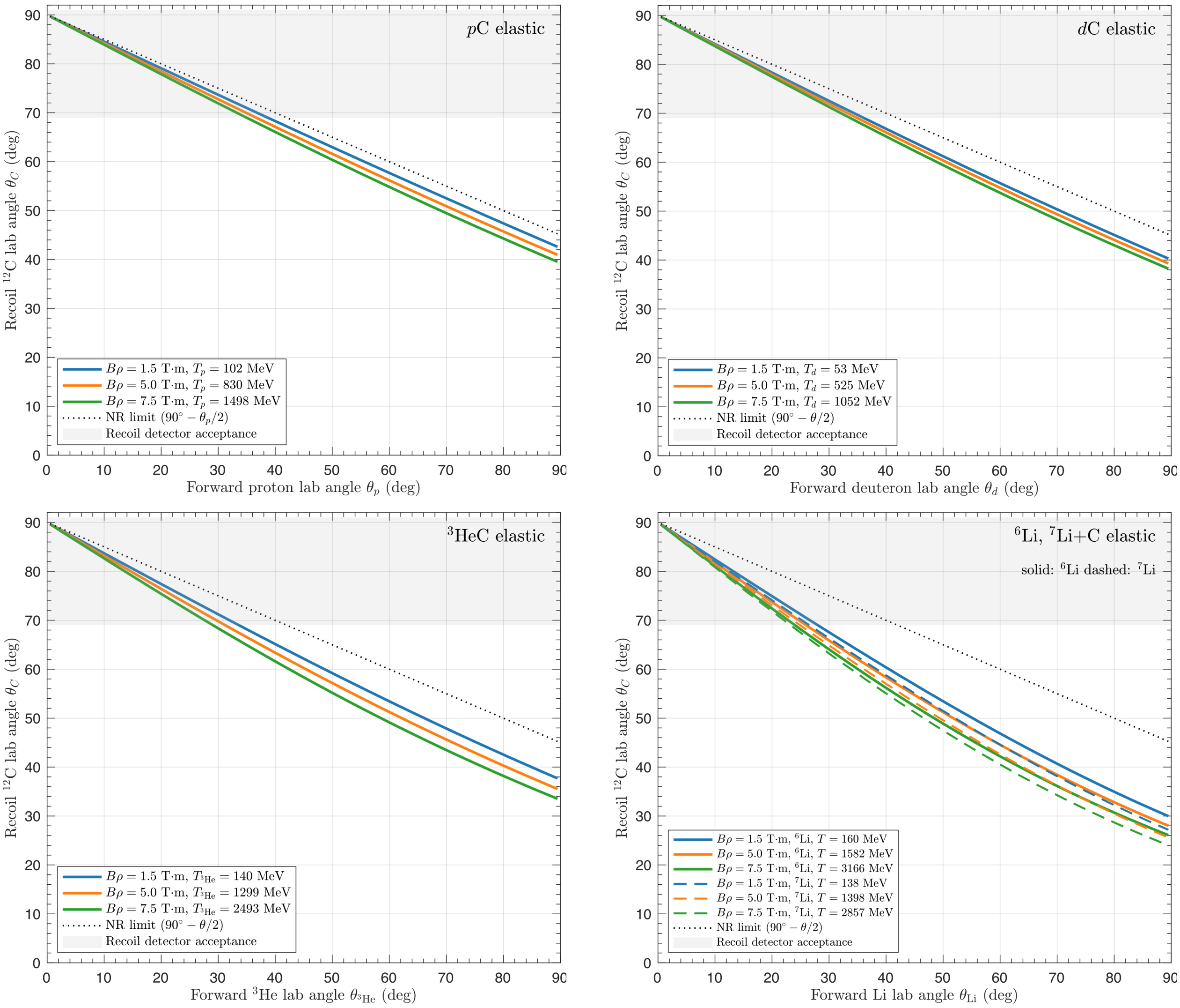

Figure 1: Elastic scattering kinematics for polarized beam species on a ^{12}C target: recoil carbon lab angle θ_C as a function of the forward beam lab angle, at three magnetic rigidities $B\rho = 1.5, 5.0,$ and $7.5\,\mathrm{T\,m}$ spanning the Booster acceleration range. The corresponding beam kinetic energies are given in the legends. The gray band marks the recoil ring detector acceptance ($\theta_C = 69.0^\circ$–91.3°). The dotted line shows the non-relativistic billiard limit $\theta_C = 90^\circ - \theta/2$. Top left: pC. Top right: dC. Bottom left: ^{3}HeC. Bottom right: ^{6}Li+C and ^{7}Li+C (solid and dashed, respectively). The kinematics of all species are compatible with a single fixed recoil-ring detector geometry across the full Booster rigidity range.

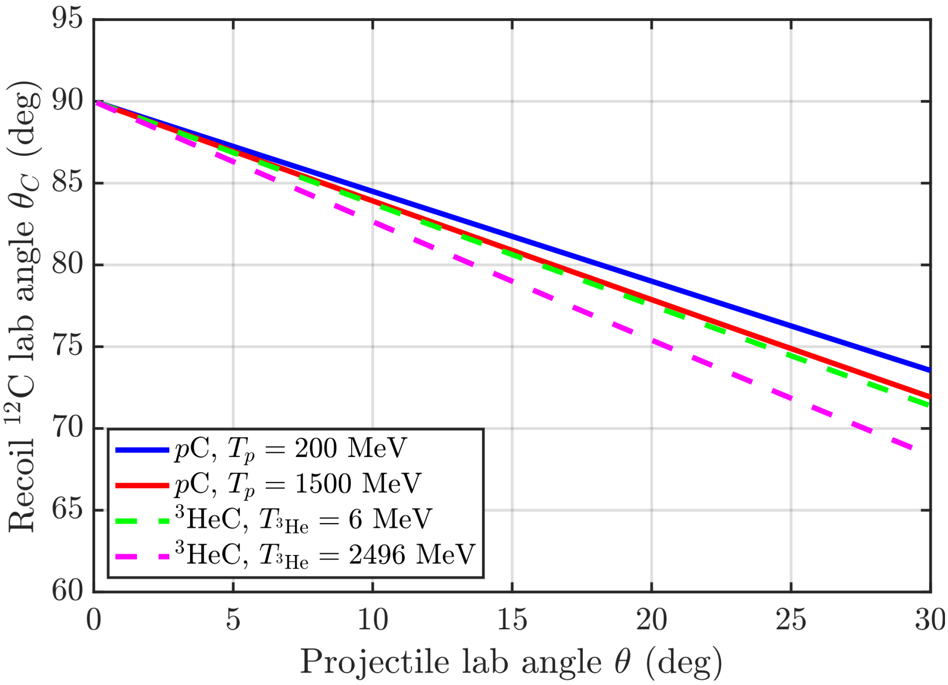

Figure 2: Laboratory recoil angle θ_C of the elastic carbon recoil as a function of the projectile laboratory scattering angle θ for pC and ^{3}HeC elastic scattering at Booster injection and extraction energies. The proton beam energies correspond to $T_p = 200\,\mathrm{MeV}$ and $1.5\,\mathrm{GeV}$, and the ^{3}He ion beam energies correspond to $T_{^3\mathrm{He}} = 2\,\mathrm{MeV/u}$ and $832\,\mathrm{MeV/u}$, as listed in Table 1. Over the full Booster energy range and for projectile scattering angles up to 30°, the recoil carbon nuclei emerge in a narrow angular interval near 70° to 90°. This weak dependence on beam species and beam energy allows a fixed recoil detector geometry to provide complete acceptance for both proton and ^{3}He ion beam polarimetry.

extend far beyond 100 MeV at the highest Booster energies. The horizontal lines in Fig. 3 indicate the approximate maximum recoil energies that can be fully stopped in silicon detectors of thickness 300 µm and 500 µm, respectively. These limits show that a 500 µm detector provides full stopping capability over most of the recoil angular range relevant for pC polarimetry, while the innermost strips at the smallest recoil angles operate in ΔE mode.

For ^{3}HeC the recoil energies extend beyond the 500 µm stopping range at the highest Booster energies, and the detector operates as a ΔE element in that regime.

An important conclusion from Fig. 3 is that for pC elastic scattering the recoil carbon nuclei can be fully stopped in silicon detectors of thickness 500 µm over most of the recoil angular range relevant for Booster polarimetry. Full stopping allows measurement of the total recoil kinetic energy T_C, and together with the measured recoil angle θ_C provides a strict kinematic constraint for elastic scattering. Elastic events populate a narrow and well-defined correlation between T_C and θ_C, while inelastic reactions do not satisfy this relation and can therefore be efficiently rejected using recoil information alone. For ^{3}HeC elastic scattering, the recoil carbon energies extend to significantly higher values at Booster extraction energy, and even a 500 µm detector does not fully stop the recoil carbon nuclei over the entire angular range. As a result, the elastic identification based on recoil information alone becomes less selective. However, detection of the forward scattered ^{3}He ion beam particle in coincidence provides an additional kinematic constraint through the measured forward scattering angle. The combined measurement of recoil carbon and forward ^{3}He restores the ability to cleanly identify elastic events, providing event selection quality comparable to that achieved for pC elastic scattering using fully stopped recoil carbon nuclei.

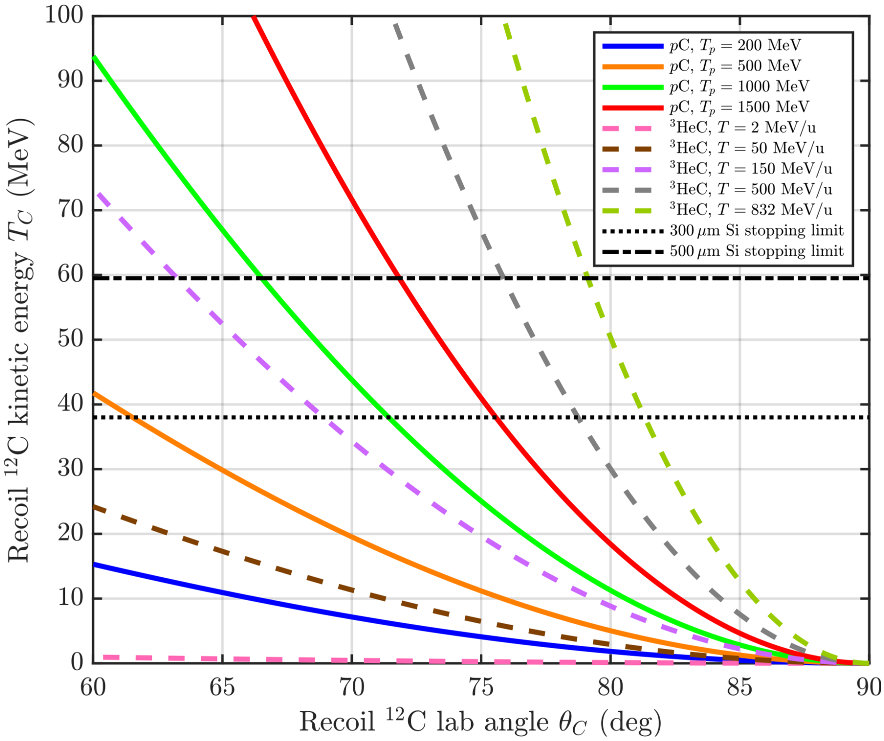

Figure 3: Recoil carbon kinetic energy T_C as a function of recoil laboratory angle θ_C for pC and ^{3}HeC elastic scattering over the full Booster energy range listed in Table 1. The horizontal lines indicate the maximum recoil energies that can be fully stopped in silicon detectors of thickness 300 µm ($T_C \leq 38$ MeV) and 500 µm ($T_C \leq 59$ MeV), based on SRIM-2013 calculations [13]; see Sec. 4.5 for details.

3 Data Situation for pC and ^{3}HeC Elastic Scattering

The polarimeter performance depends on the availability of experimental data for the differential cross section and analyzing power A_y for elastic scattering in the Booster energy range. These quantities determine the expected event rates, the achievable statistical precision, and the sensitivity of the polarimeter. Since a pC polarimeter already exists at 200 MeV behind the Linac, the primary emphasis here is on the higher energies approaching Booster extraction. In addition, the available data for ^{3}HeC elastic scattering in the Booster energy range must be assessed to establish the feasibility of polarized ^{3}He measurements.

3.1 pC Elastic Scattering

Elastic pC scattering has been studied extensively over a wide range of beam energies. Differential cross section and analyzing power data exist in the energy region relevant for Booster operation, including energies approaching and exceeding 1.5 GeV. These data provide the basis for predicting the recoil carbon angular and energy distributions and for determining the analyzing power accessible to the Booster polarimeter.

For quantitative Booster polarimeter performance estimates we require both the analyzing power A_y and the differential yield for pC scattering in the angular domain relevant for recoil-carbon detection. In the present context, we restrict the projectile laboratory scattering angle to $\theta \leq 30°$, which corresponds to recoil-carbon laboratory angles $\theta_C \simeq 70°$ to $90°$ as established by the elastic kinematics in Sec. 2 and Fig. 2. The analyzing power is described by the Bonin parametrization [14], which extends the McNaughton form [4] and provides an analytic representation of A_y as a function of beam momentum and scattering angle in the energy range relevant for the Booster. In this approach, A_y is expressed in terms of a smooth function of θ with momentum-dependent coefficients, fitted to a large body of proton–carbon polarization data and constrained by dedicated measurements [3, 15]. In addition to A_y, the event yield must be modeled through the differential cross section, or an equivalent differential efficiency. Bonin et al. [14] provide an analytic parametrization of the inclusive pC scattering yield in the momentum range relevant for the Booster, which can be used as a practical surrogate for $d\sigma/d\Omega$ for rate estimates and optimization of the polarimeter acceptance.

The angular region of optimal polarimeter performance is determined by the figure of merit,

$$\mathrm{FOM}(\theta) = A_y^2(\theta)\,\frac{d\sigma}{d\Omega}(\theta), \tag{11}$$

which quantifies the statistical power per unit solid angle. For a fixed incident flux and target thickness, the statistical uncertainty of a polarization measurement scales approximately as $\delta P \propto 1/\sqrt{\int \mathrm{FOM}(\theta)\,d\Omega}$, and the measuring time required to reach a given statistical precision scales inversely with the acceptance-weighted figure of merit, $t \propto 1/\int \mathrm{FOM}(\theta)\,d\Omega$. Maximizing the FOM therefore minimizes the required measuring time and defines the optimal angular region for polarimeter operation. In the following we therefore generate, at representative Booster energies $T_p = 500\,\mathrm{MeV}$, $850\,\mathrm{MeV}$, and $1.2\,\mathrm{GeV}$, the three key curves $d\sigma/d\Omega(\theta)$, $A_y(\theta)$, and $\mathrm{FOM}(\theta)$ over $\theta \leq 30°$. These plots establish the angular interval where the recoil-carbon polarimeter is most efficient and provide the input needed to define the detector placement and segmentation in the kinematic region discussed in Sec. 2.

3.2 Parametrization of analyzing power and differential cross section for pC scattering

For quantitative modeling of the Booster polarimeter performance, analytic parametrizations of the analyzing power $A_y(\theta, p)$ and the differential cross section $d\sigma/d\Omega(\theta, p)$ are required. In this work we adopt the parametrizations given by Bonin *et al.* [14], which extend the McNaughton form [4] and reproduce the available experimental data over the proton momentum range $p = 1.0\,\mathrm{GeV/c}$ to $2.0\,\mathrm{GeV/c}$, corresponding to kinetic energies relevant for the Booster. The Bonin parametrization is based on inclusive p+C measurements in a thick target configuration, where elastic and quasi-elastic contributions, including excitations of low-lying nuclear states such as the 2^+ level at $4.44\,\mathrm{MeV}$, are not experimentally separated. Consequently, the resulting $A_y(\theta, p)$ and $d\sigma/d\Omega(\theta, p)$ represent effective quantities that already incorporate the combined contributions of elastic and inelastic scattering channels.

3.2.1 Analyzing power

The analyzing power is parametrized as

$$A_y(\theta, p) = \frac{a(p')r}{1 + b(p')r^2 + c(p')r^4} + d(p')p\sin(5\theta), \tag{12}$$

where

$$r = p\sin\theta, \tag{13}$$

and

$$p' = p - 1.4\,\mathrm{GeV}\,{c_0}^{-1}. \tag{14}$$

The coefficient functions are third-order polynomials,

$$a(p') = \sum_{i=0}^{3} a_i p'^i, \qquad b(p') = \sum_{i=0}^{3} b_i p'^i, \tag{15}$$

$$c(p') = \sum_{i=0}^{3} c_i p'^i, \qquad d(p') = \sum_{i=0}^{3} d_i p'^i, \tag{16}$$

with numerical values given in Table 2. For the thin carbon targets used in the Booster storage ring, the proton momentum p corresponds to the incident beam momentum.

Table 2: Coefficients of the Bonin parametrization of the analyzing power $A_y(\theta, p)$ [14]. The value of c_3 corrects a sign error in the original publication.

i	a_i	b_i	c_i	d_i
0	1.626	14.909	574.719	0.1275
1	−1.786	−0.594	−560.410	0.0550
2	1.933	−91.766	−610.026	−0.138
3	−0.285	207.064	1154.66	−0.639

3.2.2 Differential cross section

Bonin *et al.* parametrized the differential efficiency $\varepsilon(\theta, e_c, p)$, defined as the number of scattering events per incident proton per degree of scattering angle,

$$\varepsilon(\theta, e_c, p) = n \frac{d\sigma}{d\Omega}(\theta, p)\, 2\pi \sin\left(\theta \frac{\pi}{180}\right), \tag{17}$$

where

$$n = \frac{\rho_c e_c N_A}{A_C} \tag{18}$$

is the number of carbon nuclei per unit area, with $\rho_c = 2.267\,\mathrm{g\,cm^{-3}}$, $N_A = 6.022\,140\,76 \times 10^{23}\,\mathrm{mol^{-1}}$, and $A_C = 12\,\mathrm{g\,mol^{-1}}$.

Solving Eq. (17) for the differential cross section gives

$$\frac{d\sigma}{d\Omega}(\theta, p) = \frac{1}{2\pi \sin(\theta\pi/180)} \frac{1}{n}\, \epsilon(\theta, p). \tag{19}$$

Using the parametrization of ε and extracting the microscopic cross section yields the analytic form

$$\frac{d\sigma}{d\Omega}(\theta, p) = G(p) \exp\bigl(B\theta + C\theta^2 + D\theta^3\bigr), \tag{20}$$

where θ is the scattered proton laboratory angle in ° and

$$G(p) = G_0 + G_1 p + G_2 p^2. \tag{21}$$

The coefficients B, C, D were fitted by Bonin *et al.* with θ expressed in degrees (Table 3 of Ref. [14]). The exponential attenuation factor $\exp(-e_c/L(p))$ introduced by Bonin to describe thick analyzer blocks is omitted here, since the microscopic differential cross section itself is independent of target thickness and directly applicable to the thin carbon targets used in the Booster storage ring. The coefficients of the parametrization are given in Table 3.

Equations (12) and (20) provide a complete analytic description of the angular dependence of the analyzing power and differential cross section in the Booster energy range and form the basis for the polarimeter performance calculations presented in the following sections.

Table 3: Coefficients of the Bonin parametrization of the differential cross section, Eq. (20), taken from Table 3 of Ref. [14]. The coefficients B, C, D apply with θ in degrees, their units are deg^{-1}, deg^{-2}, and deg^{-3} respectively. The G coefficients have units of $\mathrm{cm}^2\,\mathrm{sr}^{-1}$ (times the appropriate power of GeV/c for G_1 and G_2), p is in GeV/c.

Parameter	Unit	Value
B	deg^{-1}	-0.880
C	deg^{-2}	5.67×10^{-2}
D	deg^{-3}	-1.39×10^{-3}
G_0	$\mathrm{cm}^2\,\mathrm{sr}^{-1}$	-2.98×10^{-23}
G_1	$\mathrm{cm}^2\,\mathrm{sr}^{-1}\,(\mathrm{GeV/c})^{-1}$	9.32×10^{-23}
G_2	$\mathrm{cm}^2\,\mathrm{sr}^{-1}\,(\mathrm{GeV/c})^{-2}$	-2.39×10^{-24}

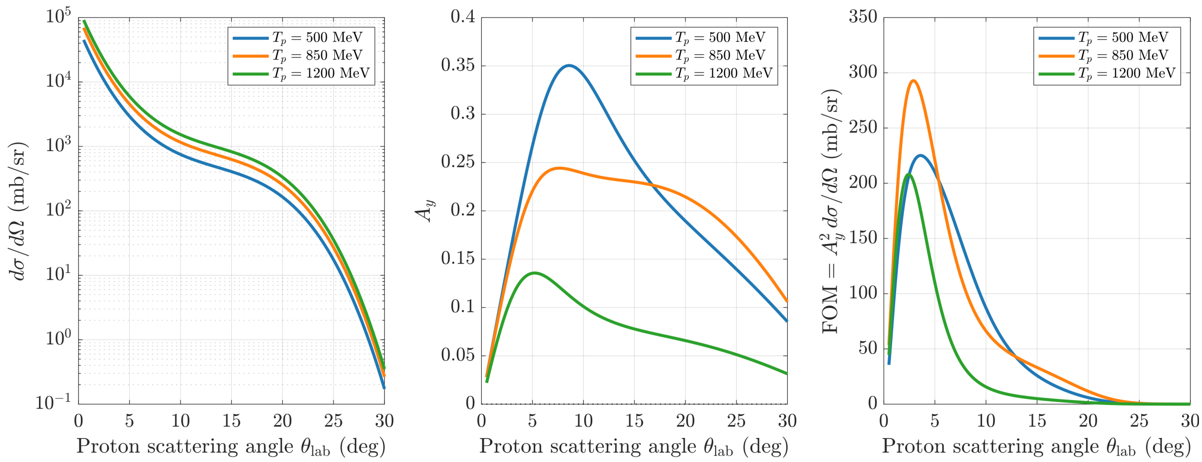

Figure 4: Differential cross section $d\sigma/d\Omega$, analyzing power A_y, and figure of merit FOM $= A_y^2\, d\sigma/d\Omega$ for elastic pC scattering as a function of the laboratory scattering angle of the proton, θ_p^{lab}. The curves are calculated using the parametrization of Bonin *et al.* [14] for proton kinetic energies $T_p = 500\,\mathrm{MeV}$, $850\,\mathrm{MeV}$, and $1.2\,\mathrm{GeV}$, covering the Booster energy range. The differential cross section is shown in absolute units of $\mathrm{mb\,sr}^{-1}$ appropriate for thin carbon targets. The maximum of the figure of merit occurs in the angular range $\theta_p^{\mathrm{lab}} \approx 1^\circ$ to 10°, which defines the optimal angular region for polarization measurements and guides the detector placement discussed in Sec. 2.

3.2.3 Implications of the figure of merit for Booster polarimetry

The figure of merit [Eq. (11)] quantifies the statistical power per unit solid angle and directly determines the achievable statistical precision of a polarization measurement.

For a beam of intensity I, a carbon target with areal density d_t, and a detector covering solid angle $\Delta\Omega$, the event rate is

$$R(\theta) = I\, d_t\, \frac{d\sigma}{d\Omega}(\theta)\, \Delta\Omega, \tag{22}$$

and the statistical uncertainty of the polarization measurement is

$$\delta P = \frac{1}{A_y \sqrt{N}}, \tag{23}$$

where $N = R\,t$ is the number of detected elastic scattering events accumulated during measurement time t. Combining these expressions gives

$$\delta P = \frac{1}{\sqrt{I\, d_t\, \Delta\Omega\, t\, \mathrm{FOM}}}, \tag{24}$$

demonstrating that the statistical precision improves with increasing FOM. Inverting Eq. (24), the time required to accumulate sufficient statistics to reach a given absolute precision δP on the polarization is

$$t_{\mathrm{dwell}} \propto \frac{1}{\mathrm{FOM} \cdot (\delta P)^2}, \tag{25}$$

where t_{dwell} is the dwell time, defined as the time during which the carbon target is held at a fixed transverse position relative to the beam and elastic scattering events are accumulated. Maximizing the acceptance-averaged FOM directly minimizes t_{dwell}, and halving δP requires four times longer accumulation. The dwell time is evaluated quantitatively in Sec. 5.4 once the beam parameters and geometric overlap of beam and target have been established. The above expressions are schematic and assume that $d\sigma/d\Omega$ and A_y are approximately constant over the accepted solid angle. In the quantitative performance estimates below, the corresponding acceptance-averaged quantities are used instead (Sec. 5.6.3).

The angular dependence of the FOM calculated using the Bonin parametrization is shown in Fig. 4. The FOM peaks in the range $\theta_p^{\mathrm{lab}} \approx 1^\circ$ to 10° and shifts toward smaller angles with increasing beam momentum, reflecting the forward concentration of the differential cross section at higher energies. For pC polarimetry, however, the recoil ring alone is sufficient: the recoil carbon at $\theta_C \approx 80^\circ$ provides a clean elastic event sample through the T_C-θ_C kinematic correlation without requiring a forward coincidence, and the acceptance-averaged FOM integrated over the recoil ring is adequate for a statistically precise polarization measurement within a single Booster cycle, as demonstrated in Sec. 5.4.

3.3 Existing ^{3}HeC elastic scattering data in the Booster energy range

In the Booster energy range, ^{3}HeC elastic polarimetry requires experimental input for the analyzing power A_y and the differential cross section $d\sigma/d\Omega$ at representative ion-beam energies. A suitable low-energy anchor point is provided by Kamiya *et al.* [10], who measured the differential cross section and induced polarization for elastic scattering of a ^{3}He ion beam from ^{12}C at an incident kinetic energy $E_{^3\mathrm{He}} = 443\,\mathrm{MeV}$. These data are particularly relevant because the Booster injection energy for ^{3}He is comparatively low, and $E_{^3\mathrm{He}} = 443\,\mathrm{MeV}$ lies in the lower part of the Booster acceleration cycle where an additional in-ring polarization reference point is desirable.

The paper reports the differential cross section $d\sigma/d\Omega(\theta_{\mathrm{cm}})$ in Fig. 4 and the induced polarization $P_y(\theta_{\mathrm{cm}})$ in Fig. 5 (lower-left panel) for the ^{3}He+^{12}C system. For a spin-$\frac{1}{2}$ projectile on a spin-0 target, the induced polarization of the scattered projectile equals the analyzing power for a transversely polarized incident beam under time-reversal invariance, so the data of Fig. 5 can be used directly as

$$A_y(\theta_{\mathrm{cm}}) = P_y(\theta_{\mathrm{cm}}). \tag{26}$$

Together with the measured $d\sigma/d\Omega$, this enables a quantitative estimate of the polarimetric performance at this energy via the figure of merit from Eq. (11).

Kamiya *et al.* provide the underlying optical-model framework and parametrizations of both the differential cross section and the induced polarization as functions of the center-of-mass scattering angle. In principle, these parametrizations allow direct calculation of the analyzing power and differential cross section at $E_{^3\mathrm{He}} = 443\,\mathrm{MeV}$, however, we use data digitized from Figs. 4 and 5 of Ref. [10] and convert them to the laboratory frame for the polarimeter performance estimate. Using the elastic two-body kinematics derived in Sec. 2, the center-of-mass angle can be converted to the laboratory angles and recoil energies relevant for the Booster polarimeter. This provides the quantitative input required to evaluate the figure of merit via Eq. (11) and to assess the achievable polarimeter performance at this energy.

Table 4: Kinematic quantities for elastic $^3\mathrm{He}^{++} + {}^{12}\mathrm{C}$ scattering at $T_{^3\mathrm{He}} = 443\,\mathrm{MeV}$. The $^3\mathrm{He}^{++}$ mass is the bare helion mass from CODATA 2018 [11].

Quantity	Symbol	Unit	Value
$^3\mathrm{He}^{++}$ mass	m_1	MeV/c^2	2808.391
$^{12}\mathrm{C}$ mass	m_2	MeV/c^2	11177.9
Invariant mass	$\sqrt{s}$	MeV	14336
CM frame velocity	β_cm	–	0.1135
CM frame boost	γ_cm	–	1.0065
CM momentum	p_cm	MeV/c	1278
Projectile CM speed	β_p	–	0.4141
Velocity ratio	$r = \beta_\mathrm{cm}/\beta_p$	–	0.274

3.3.1 Differential cross section, analyzing power, and figure of merit at 443 MeV

The differential cross section $d\sigma/d\Omega(\theta_\mathrm{cm})$ and analyzing power $A_y(\theta_\mathrm{cm})$ reported by Kamiya et al. [10] were digitized from Figs. 4 and 5 of that reference and converted to the laboratory frame for use in the polarimeter performance estimate.

The center-of-mass and laboratory scattering angles are related through the relativistic two-body kinematics derived in Sec. 2, which we briefly summarize here for completeness. For elastic scattering of a projectile of mass m_1 and kinetic energy T from a target nucleus of mass m_2 at rest, the invariant mass of the system is

$$\sqrt{s} = \sqrt{m_1^2 + m_2^2 + 2m_2(T + m_1)}, \tag{27}$$

and the velocity and Lorentz factor of the center-of-mass frame in the laboratory are

$$\beta_\mathrm{cm} = \frac{p_1}{E_1 + m_2}, \qquad \gamma_\mathrm{cm} = \frac{E_1 + m_2}{\sqrt{s}}, \tag{28}$$

where $E_1 = T + m_1$ and $p_1 = \sqrt{E_1^2 - m_1^2}$ are the total energy and momentum of the projectile in the laboratory. The center-of-mass momentum of the projectile is

$$p_\mathrm{cm} = \frac{m_2\, p_1}{\sqrt{s}}, \tag{29}$$

and the speed of the projectile in the center-of-mass frame is

$$\beta_p = \frac{p_\mathrm{cm}}{E_{1,\mathrm{cm}}}, \qquad E_{1,\mathrm{cm}} = \sqrt{p_\mathrm{cm}^2 + m_1^2}. \tag{30}$$

The laboratory scattering angle θ_lab of the projectile is related to the center-of-mass angle θ_cm by

$$\tan\theta_\mathrm{lab} = \frac{\sin\theta_\mathrm{cm}}{\gamma_\mathrm{cm}(\cos\theta_\mathrm{cm} + r)}, \tag{31}$$

where $r = \beta_\mathrm{cm}/\beta_p$. For $^3\mathrm{He}$ on $^{12}\mathrm{C}$ at $T = 443\,\mathrm{MeV}$ the relevant kinematic quantities are summarized in Table 4. Since $r < 1$, the mapping between center-of-mass and laboratory angles is unique over the full angular range.

The differential cross section in the laboratory frame is obtained from the center-of-mass cross section via the Jacobian of the solid angle transformation,

$$\left.\frac{d\sigma}{d\Omega}\right|_\mathrm{lab} = \left.\frac{d\sigma}{d\Omega}\right|_\mathrm{cm} \cdot \frac{d\Omega_\mathrm{cm}}{d\Omega_\mathrm{lab}}, \tag{32}$$

where

$$\frac{d\Omega_\mathrm{cm}}{d\Omega_\mathrm{lab}} = \frac{\left(1 + 2r\cos\theta_\mathrm{cm} + r^2\right)^{3/2}}{\gamma_\mathrm{cm}^2\,\left(1 + r\cos\theta_\mathrm{cm}\right)^2}. \tag{33}$$

The analyzing power A_y is a ratio of cross sections and is therefore frame-invariant; no Jacobian is required.

The digitized data converted to the laboratory frame are shown in Fig. 5. The left panel shows the differential cross section $d\sigma/d\Omega_{\rm lab}$ as a function of the laboratory scattering angle of the ^{3}He ion. The cross section falls steeply with angle, spanning nearly six orders of magnitude from the most forward angles accessible to approximately 20°. The center panel shows the analyzing power $A_y(\theta_{\rm lab})$, which exhibits two local maxima separated by a shallow minimum. The larger-angle maximum lies within the present forward-detector acceptance, while the lower-angle maximum is just below its inner edge. The right panel shows the figure of merit FOM $= A_y^2\, d\sigma/d\Omega$, which determines the statistical efficiency of the polarimeter per unit solid angle. The dual x-axis in each panel gives both the laboratory angle and the corresponding center-of-mass angle connected through Eq. (31).

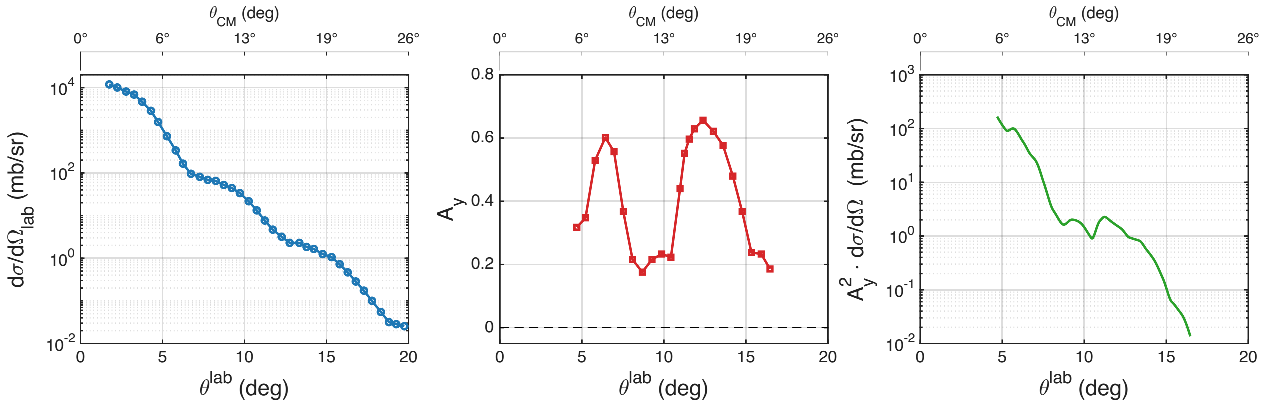

Figure 5: Differential cross section $d\sigma/d\Omega$, analyzing power A_y, and figure of merit FOM $= A_y^2\, d\sigma/d\Omega$ for elastic $^3\mathrm{He} + {}^{12}\mathrm{C}$ scattering at $T_{^3\mathrm{He}} = 443\,\mathrm{MeV}$ as a function of the ^{3}He laboratory scattering angle. Data are digitized from Kamiya et al. [10] and converted to the laboratory frame using the relativistic kinematics described in the text. The upper x-axis gives the corresponding center-of-mass scattering angle. The analyzing power exhibits two local maxima, with the larger-angle maximum lying within the present forward-detector acceptance.

3.4 dC Elastic Scattering

The spin dynamics of a particle in a circular accelerator are governed by the Thomas-BMT equation, in which the magnetic anomaly

$$G = \frac{g-2}{2} \tag{34}$$

determines the spin tune $\nu_s = G\gamma$. The g-factor is defined by

$$\vec{\mu} = g\frac{q}{2m}\vec{S}, \tag{35}$$

where $\vec{S}$ is the spin vector in units of $\hbar$ with $|\vec{S}| = I\hbar$, $q = Ze$, and $m = Am_p$. Expressing the magnetic moment in units of the nuclear magneton $\mu_N = e\hbar/2m_p$ gives

$$g = \frac{A\,\mu}{Z\,I\,\mu_N}. \tag{36}$$

The values of g and G for the beam species relevant to Booster polarimetry are summarized in Table 5.

Depolarizing resonances occur when the spin precession frequency becomes commensurate with the orbital motion. The two main classes of resonances are imperfection resonances, driven by

Nucleus	Z	A	I	m (MeV/c^2)	μ (μ_N)	$g = A\mu/(ZI\mu_N)$	$G = (g-2)/2$
p	1	1	1/2	938.272	+2.7928	+5.5856	+1.7928
^{3}He	2	3	1/2	2808.391	−2.1276	−6.3828	−4.1914
d	1	2	1	1875.613	+0.8574	+1.7148	−0.1426
^{6}Li	3	6	1	5601.518	+0.8220	+1.6440	−0.1780
^{7}Li	3	7	3/2	6533.832	+3.2564	+5.0648	+1.5324

Table 5: Spin and magnetic properties relevant for spin dynamics in circular accelerators, using the BMT definition $g = A\mu/(ZI\mu_N)$ and $G = (g-2)/2$. Nuclear masses are fully stripped ion (bare nucleus) values; proton, deuteron, and helion masses from CODATA 2018 [11]; ^{6,7}Li nuclear masses from AME2020 [16]. Magnetic moments from [17]; proton and deuteron values from CODATA [11].

magnet errors and closed-orbit distortions, which occur when

$$\nu_s = k, \qquad k \in \mathbb{Z}, \tag{37}$$

and intrinsic resonances, driven by the focusing fields seen by a particle undergoing betatron oscillations, which occur when

$$\nu_s = kP \pm Q_{x,y}, \tag{38}$$

where P is the superperiodicity of the lattice and $Q_{x,y}$ are the horizontal and vertical betatron tunes.

For the deuteron, $G_d = -0.1426$ is unusually small compared to other species in Table 5. As a result, the spin tune $\nu_s = G_d\gamma$ remains well below unity throughout the entire Booster acceleration cycle, and neither the imperfection resonance condition Eq. (37) nor the intrinsic resonance condition Eq. (38) can be satisfied. Polarized deuterons can therefore be accelerated through the full Booster energy range without crossing any depolarizing resonances [18], making the deuteron the most favorable species for polarized beam acceleration in the Booster.

The analyzing power for elastic dC scattering is well measured over the Booster energy range. Satou et al. [19] measured cross sections and vector and tensor analyzing powers A_y and A_{yy} for elastic and inelastic deuteron scattering from ^{12}C at 270 MeV, providing a well-established reference point near the middle of the Booster energy range. Müller et al. [20] extended the world data set with vector analyzing power measurements at seven kinetic beam energies between 170 and 380 MeV at COSY, using a thin diamond-strip carbon target with forward scintillator and straw-tube detectors; excellent agreement with the existing data at 200 and 270 MeV was found. At higher momenta, the same group demonstrated efficient dC polarimetry at COSY with $p = 0.97$ GeV/c using a calorimetric LYSO polarimeter [21], establishing that forward elastic dC scattering remains a practical analyzing reaction up to momenta approaching Booster extraction. Together these measurements provide a solid experimental basis for dC polarimetry across the full Booster energy range, comparable in quality to the pC data situation.

3.5 ^{6,7}LiC Elastic Scattering

Polarized ^{6}Li and ^{7}Li beams are potential future species for the EIC injector chain. Both isotopes exhibit pronounced α-cluster structure,

$$^6\mathrm{Li} \approx \alpha + d, \qquad ^7\mathrm{Li} \approx \alpha + t, \tag{39}$$

with the α core carrying no spin, so the nuclear spin and magnetic properties are dominated by the deuteron or triton cluster respectively, and the resulting G values are given in Table 5.

For ^{6}Li, $G_{^6\mathrm{Li}} = -0.178$ is close to the deuteron value $G_d = -0.143$, reflecting the dominant role of the deuteron cluster in determining the magnetic properties of ^{6}Li. The spin dynamics during Booster acceleration are therefore similarly favorable, with few depolarizing resonances encountered.

For ^{7}Li, $G_{^7\mathrm{Li}} = +1.532$ is close to the proton value $G_p = +1.793$, so polarized ^{7}Li acceleration faces a resonance density comparable to that of the proton and would require similar mitigation strategies. The nuclear magnetic moment receives contributions from both the spin and orbital motion of the triton cluster around the α core,

$$\vec{\mu} = g_l \, \vec{l} + g_s \, \vec{s}, \tag{40}$$

and for the $J^\pi = 3/2^-$ ground state with $l = 1$ these contributions do not cancel strongly in the BMT convention, resulting in a G value an order of magnitude larger than the deuteron or ^{6}Li.

For LiC elastic polarimetry the same recoil-carbon detector geometry applies without modification, since the kinematic arguments of Sec. 2 depend only on the projectile-to-carbon mass ratio and magnetic rigidity. For ^{6}Li, vector analyzing power measurements on ^{12}C extend up to 150 MeV [22], while for ^{7}Li only unpolarized differential cross sections have been measured at intermediate energies [23]; in neither case do data exist in the Booster energy range. The Booster polarimeter is therefore identified as a potential instrument for mapping the LiC analyzing power, in direct analogy to the role foreseen for ^{3}HeC polarimetry described in Sec. 3.3.

4 Polarimeter Design

4.1 Measurement concept and event identification

The Booster polarimeter is based on elastic nuclear scattering of the circulating beam from a thin internal carbon target, with detection of the recoil ^{12}C nucleus. The transverse beam polarization is determined from the azimuthal asymmetry of the recoil carbon yield, which is modulated by the analyzing power A_y of the elastic reaction according to

$$\frac{dN}{d\phi} = N_0(\theta, \phi) \left[1 + A_y(\theta) \left(P_y \cos\phi - P_x \sin\phi\right)\right], \tag{41}$$

where $N_0(\theta, \phi)$ is the azimuthally symmetric unpolarized yield, $A_y(\theta)$ is the analyzing power, P_y and P_x are the vertical and horizontal components of the transverse beam polarization, and ϕ is the azimuthal angle of the recoil nucleus measured positive from the x-axis toward y. The sign convention follows from the normal to the scattering plane $\hat{n} = (-\sin\phi, \cos\phi, 0)$, giving $\vec{P} \cdot \hat{n} = P_y \cos\phi - P_x \sin\phi$. The polarization components are extracted from the amplitudes of the $\cos\phi$ and $\sin\phi$ modulations of the recoil yield after integrating over θ within the detector acceptance. Since the recoil carbon emerges at azimuthal angle ϕ_C opposite to the scattered projectile, the scattering plane normal constructed from the recoil direction satisfies $\hat{n}_{\mathrm{recoil}} = -\hat{n}_{\mathrm{forward}}$; the analyzing power A_y in Eq. (41) must therefore be taken with opposite sign when the Bonin or McNaughton parametrizations, which are based on forward proton detection, are used directly.

The coordinate system used throughout this section is beam-based: the z-axis points along the beam direction, y is vertical (upward), x is horizontal. The polar angle θ is measured from z and the azimuthal angle ϕ from the x-axis toward y. Recoil carbon angles θ_C and forward scattering angles θ are both defined in the laboratory frame.

Each silicon pad detector is segmented into strips. In the recoil ring the strips run radially, subdividing the azimuthal dimension of each station and providing a measurement of ϕ. Since θ_C is already determined by the energy deposit T_C through the elastic kinematic relation in Eqs. (8) and (9), no strip segmentation in the polar direction is required. In the forward ring the strips run azimuthally, subdividing the radial dimension of each station and providing a measurement of θ for the kinematic coincidence constraint. The azimuthal position of a forward hit is determined by which station fired, in the same way as for the recoil ring.

4.1.1 Elastic event identification for pC scattering

For elastic pC scattering the two-body kinematics fully constrain the event through the recoil carbon angle alone. As established in Sec. 2, the recoil ^{12}C nucleus is confined to laboratory angles $\theta_C \approx 70°$–$90°$ over the full Booster energy range, and its kinetic energy T_C is uniquely determined by θ_C through the elastic kinematic relations in Eqs. (8) and (9). A measured pair (θ_C, T_C) lying on the elastic locus in the T_C–θ_C plane therefore identifies an elastic event without requiring detection of the scattered proton. The recoil detector ring alone is thus sufficient for clean elastic event selection in the pC case, and the forward detector provides an optional coincidence cross-check but is not required for the polarimetry measurement. The overall layout of the two-ring detector system is shown in Fig. 6, with the recoil ring at $z = 17.4$ mm and the forward ring at $z = 750$ mm downstream of the target.

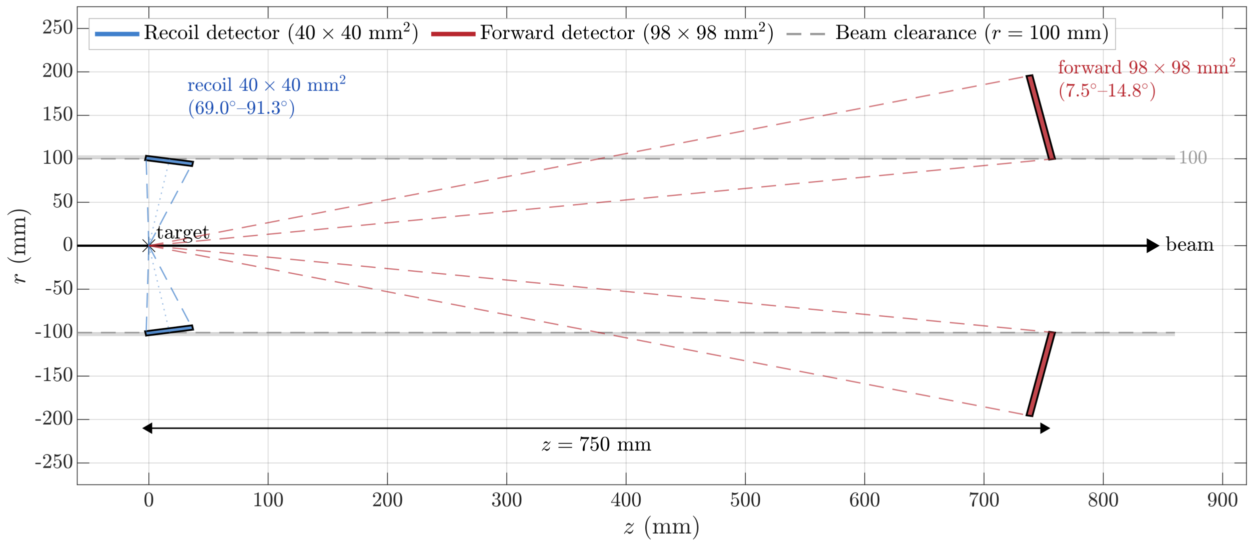

Figure 6: Side view (r–z plane) of the Booster polarimeter detector layout. The recoil detector ring (blue) has its detector-face center at $(r, z) = (100.0\,\text{mm}, 17.4\,\text{mm})$, and the forward detector ring (red) at $(r, z) = (148.1\,\text{mm}, 750.0\,\text{mm})$. In both cases the detector faces are oriented perpendicular to the line from the target to the detector-face center. The recoil ring covers the polar-angle range $\theta = 69.0°$ to $91.3°$, while the forward ring covers $\theta = 7.5°$ to $14.8°$. The dashed lines indicate the beam-clearance radius $r = \pm 100$ mm. Only one azimuthal station of each ring is shown.

4.1.2 Elastic event identification for ^{3}HeC scattering

For ^{3}He C elastic scattering, the recoil carbon signal alone is insufficient for reliable event identification. The ^{3}He nucleus has a binding energy of only 7.72 MeV, and breakup into $p+d$ or $p+p+n$ final states is energetically accessible at all Booster energies. Recoil carbon nuclei produced in breakup reactions, where one or more nucleons are emitted forward and the remainder is absorbed into the nucleus, can populate the same (θ_C, T_C) region as elastic scattering and cannot be distinguished from elastic recoils using the recoil detector alone.

Detection of the forward-scattered ^{3}He in coincidence with the recoil carbon resolves this ambiguity. In elastic scattering the forward ^{3}He angle θ and the recoil carbon angle θ_C are uniquely correlated through the two-body kinematics: for a given θ_C there is exactly one θ satisfying momentum conservation, and the measured pair (θ, θ_C) must lie on the elastic locus. Breakup events distribute projectile momentum among multiple final-state particles, violating the two-body constraint and failing the coincidence condition. The forward detector ring is therefore essential for ^{3}He C polarimetry and is the primary motivation for the two-ring detector concept described in the following subsections.

4.2 Recoil detector ring

The recoil ^{12}C nuclei are detected by a ring of six silicon pad detectors arranged azimuthally around the beam axis. The detector centers are located at a radial distance $r = 100$ mm from the beam axis and at a longitudinal position $z = 17.4$ mm downstream of the target, placing the detector-face center at a recoil angle $\theta_C = \arctan(100/17.4) \approx 80.1°$. This is close to the centroid of the elastic recoil angular distribution over the Booster energy range and corresponds to the region of large figure of merit identified in Sec. 3.2.3. The six stations are equally spaced in azimuth at $\Delta\phi = 60°$, with opposite pairs oriented to measure the up–down and left–right components of the beam polarization.

Each detector is a $40 \times 40\,\mathrm{mm}^2$ silicon pad of 500 µm thickness. The detector faces are tilted to be perpendicular to the recoil direction at $\theta_C \approx 80°$, which maximizes the geometric efficiency and ensures that recoil tracks enter the active volume at normal incidence. With this orientation, the recoil ring covers the polar-angle range $\theta_C = 69.0°$–$91.3°$.

The recoil ^{12}C kinetic energy at $\theta_C = 70°$ ranges from $T_C \approx 7$ MeV at the Booster injection energy of $T_p = 200$ MeV to $T_C \approx 72$ MeV at the extraction energy of $T_p = 1.5$ GeV. The 500 µm silicon thickness provides a stopping range of approximately 59 MeV for ^{12}C nuclei, sufficient to fully stop recoil carbons throughout the pC operating range (as shown in Fig. 3) and allowing both the energy and position of the recoil to be measured simultaneously. This enables event-by-event elastic identification via the T_C–θ_C correlation as discussed in Sec. 4.1.1.

For ^{3}He C scattering at the Booster extraction energy of 832 MeV/u, the recoil carbon kinetic energy at $\theta_C = 70°$ reaches approximately 230 MeV, far exceeding the stopping range of 500 µm silicon. In this regime the detector operates as a ΔE element, providing a measurement of the energy deposited in the active volume together with the hit position, which is used in conjunction with the forward coincidence condition described in Sec. 4.1.2 for elastic event identification.

The azimuthal arrangement of the six recoil stations is shown in the end-on view of Fig. 7. The solid angle per station, the total geometric acceptance of the recoil ring, and the corresponding geometric parameters are summarized in Table 6.

4.3 Forward detector ring

The forward-scattered beam particles are detected by a second ring of six silicon pad detectors placed at $z = 750$ mm downstream of the target. Each detector is a $98 \times 98\,\mathrm{mm}^2$ Hamamatsu silicon pad with its inner edge at $r = 100$ mm from the beam axis, providing a beam clearance of 100 mm radius. The detector centers are at $r = 148.1$ mm, and the outer edge is at $r = 196.2$ mm. The six stations are placed at the same azimuthal positions as the recoil ring, enabling direct azimuthal coincidences between corresponding recoil and forward stations.

The angular acceptance of the forward ring spans $\theta = 7.5°$–$14.8°$ in the laboratory frame, as summarized in Table 6. The azimuthal arrangement of the six forward stations and the beam clearance are shown in the end-on view of Fig. 8.

This range samples the high-angle shoulder of the figure-of-merit distribution for ^{3}He C elastic scattering at 443 MeV (Sec. 3.3.1). The analyzing power A_y exhibits two local maxima, with the larger-angle maximum lying within the present forward-detector acceptance and the lower-angle maximum just below its inner edge.

For pC scattering the same angular range corresponds to the region of large FOM identified in Fig. 4, where the forward-scattered proton can be detected for coincidence studies or independent cross-checks.

The chamber geometry is designed to accommodate future detector upgrades without modification to the existing mechanical structure. At a later stage, a second forward ring with detectors movable

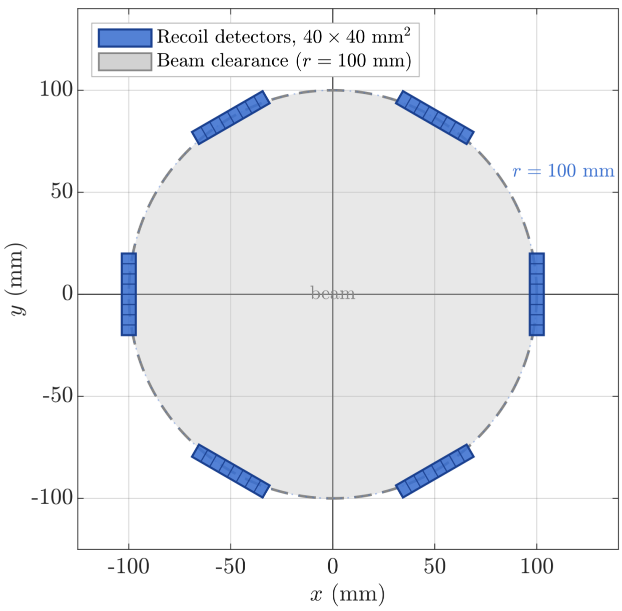

Figure 7: End-on view (x–y plane) of the recoil detector ring, looking along the beam axis. The six $40 \times 40\,\mathrm{mm}^2$ silicon pad stations have their detector-face centers arranged on a circle of radius $r = 100\,\mathrm{mm}$ with 60° azimuthal spacing. Because the detector faces are tilted in the r–z plane to point toward the target, the pad shape shown here is their projection onto the transverse plane. In the example shown, the strips run radially, subdividing each station in the azimuthal direction and thereby providing ϕ resolution across the active area, although the final choice of strip orientation or pixel size has not yet been made. For pC elastic scattering, the recoil polar angle θ_C is obtained from the measured recoil energy T_C through the elastic kinematic relation [Eqs. (8) and (9)], so radial strip segmentation is not required. The grey circle indicates the beam-clearance radius $r = 100\,\mathrm{mm}$.

closer to the beam pipe is anticipated in context to cover the smaller forward angles expected when operating with ^{6,7}Li, and with deuteron and ^{3}He beams at higher-energies.

The detector layout is shown in Figs. 6–8. The solid angle subtended by each forward station, the corresponding total geometric acceptance of the forward ring, and the geometric parameters of both detector rings are summarized in Table 6.

4.4 Kinematic constraints and elastic event selection

The elastic event selection strategy follows directly from the two-body kinematics established in Sec. 2 and is implemented through the specific detector geometry described in Secs. 4.2 and 4.3. This section quantifies the kinematic windows relevant for event selection with the actual detector positions.

4.4.1 Recoil locus for pC scattering

For elastic pC scattering the recoil ^{12}C kinetic energy at fixed θ_C varies strongly with beam energy over the Booster acceleration ramp. At the detector center $\theta_C = 80^\circ$ the elastic locus spans $T_C = 1.9\,\mathrm{MeV}$ at injection ($T_p = 200\,\mathrm{MeV}$) to $T_C = 18.4\,\mathrm{MeV}$ at extraction ($T_p = 1.5\,\mathrm{GeV}$), a factor of ten variation in recoil energy at fixed angle. Across the full angular acceptance of the recoil ring ($\theta_C = 69.0^\circ$–91.3°), the locus values are given in Table 7. At any given moment during the acceleration cycle, elastic events populate a narrow band around the instantaneous locus value, which can be tracked in real time using the known beam energy from the Booster RF system. Inelastic events, which populate a broad region below the elastic locus, are rejected by a cut on T_C

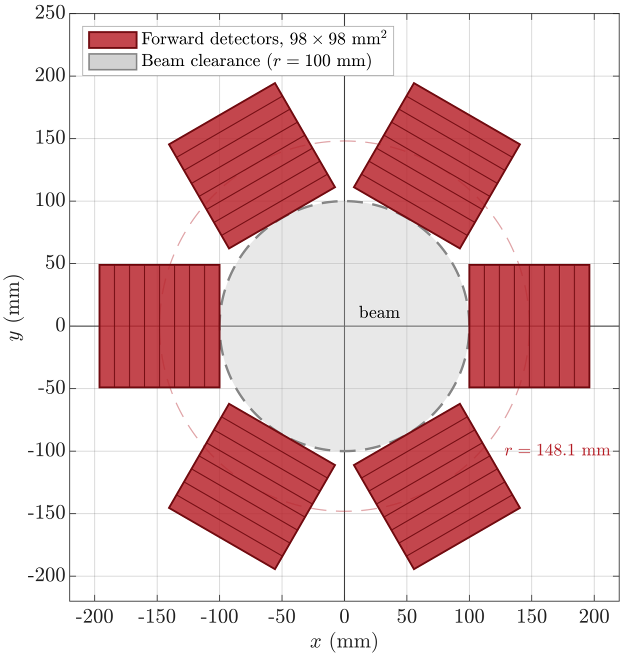

Figure 8: End-on view (x–y plane) of the forward detector ring at $z = 750\,\mathrm{mm}$, looking along the beam axis. The six $98 \times 98\,\mathrm{mm}^2$ Hamamatsu silicon pad stations are arranged with inner edges at $r = 100\,\mathrm{mm}$, set by the beam-clearance requirement, and outer edges at $r = 196.2\,\mathrm{mm}$, corresponding to a polar-angle acceptance of $\theta = 7.5°$–$14.8°$. Because the detector faces are tilted in the r–z plane to point toward the target, the pad shape shown here is their projection onto the transverse plane. In the example shown, the strips run azimuthally, subdividing each station in the radial direction and thereby providing θ resolution for the kinematic coincidence check. The azimuthal position of a forward hit is determined by which station fired. The grey circle indicates the beam-clearance radius $r = 100\,\mathrm{mm}$.

at each θ_C.

4.4.2 Forward coincidence window for ^{3}HeC scattering

For elastic $^3\mathrm{He} + {}^{12}\mathrm{C}$ scattering, event identification requires a coincidence between the recoil carbon in the recoil ring and the forward-scattered ^{3}He in the forward detector ring. The forward ring acceptance ($r = 100$–$196.2\,\mathrm{mm}$ at $z = 750\,\mathrm{mm}$, $\theta = 7.5°$–$14.8°$) defines the coincidence window. Table 8 lists the recoil carbon angle θ_C corresponding to selected forward ^{3}He angles across four beam energies spanning the Booster ramp.

The table shows that the recoil carbon angle varies only weakly with beam energy for a given θ_{fwd}, shifting by less than 1° from injection to extraction. All entries fall within the recoil ring acceptance of 69.0°–91.3°, confirming that coincidence coverage is maintained throughout the full ramp. The effective coincidence window corresponds to $\theta_C \approx 79°$–$86°$, which lies in the region of lowest recoil carbon energy and is therefore where the forward coincidence requirement is most critical for elastic event identification and background rejection.

4.5 Energy deposit and stopping in silicon

The operating mode of the recoil detector, full stopping versus ΔE, depends on whether the recoil ^{12}C nucleus is brought to rest within the 500 µm active volume. This determines the information available for elastic event identification and defines the energy resolution achievable for the T_C–θ_C kinematic constraint.

Table 6: Geometric parameters of the recoil and forward detector rings, shown in Figs. 6, 7, and 8. The detector faces are oriented perpendicular to the line from the target to the detector-face center. The quoted central azimuthal pad width uses the detector centers, while the corner azimuth angles list the four detector-corner rays as seen from the target. The solid angles are computed from the full tilted rectangular detector geometry.

Parameter	Symbol	Unit	Recoil ring	Forward ring
Number of stations	N	–	6	6
Azimuthal spacing	$\Delta\phi$	deg	60.0	60.0
Central azimuthal pad width	$\Delta\phi_{\mathrm{pad},c}$	deg	22.6	36.6
Radial center position	r	mm	100.0	148.1
Inner edge radius	r_{in}	mm	96.6	100.0
Outer edge radius	r_{out}	mm	103.4	196.2
Longitudinal position	z	mm	17.4	750.0
Detector size	–	mm^2	40×40	98×98
Silicon thickness	d	µm	500	320
Polar-angle acceptance	θ	deg	69.0–91.3	7.5–14.8
Corner azimuth angles	ϕ_{corners}	deg	-11.7, -10.9, 10.9, 11.7	-26.1, -14.0, 14.0, 26.1
Solid angle per station	$\Delta\Omega$	sr	0.150	0.016
Total solid angle	Ω	sr	0.897	0.098

Table 7: Elastic pC recoil carbon kinetic energy T_C (MeV) and forward proton scattering angle θ_p at selected recoil angles θ_C and proton beam kinetic energies spanning the Booster acceleration ramp. The values define the elastic kinematic locus used for event selection with the recoil detector ring. The quoted θ_p values are evaluated at $T_p = 1500$ MeV.

θ_C (°)	θ_p (°)	$T_p = 200$ MeV T_C (MeV)	$T_p = 500$ MeV T_C (MeV)	$T_p = 1000$ MeV T_C (MeV)	$T_p = 1500$ MeV T_C (MeV)
69	35.0	7.86	21.45	48.11	78.71
74	26.5	4.65	12.69	28.44	46.50
79	18.1	2.23	6.08	13.62	22.26
84	9.9	0.67	1.82	4.09	6.67
87	4.9	0.17	0.46	1.02	1.67
89	1.6	0.02	0.05	0.11	0.19

4.5.1 Stopping ranges for ^{12}C in silicon

The range of ^{12}C ions in silicon as a function of kinetic energy is taken from SRIM-2013 calculations [13] and is summarized in Table 9. The electronic stopping dominates throughout the energy range of interest; nuclear stopping is negligible above a few MeV. The stopping power reaches a broad maximum (Bragg peak region) around $T_C \approx 30$ MeV, with a value of approximately 0.15 MeV/µm in silicon.

The 500 µm silicon thickness fully stops ^{12}C nuclei with kinetic energies up to $T_C \approx 59$ MeV. The 300 µm alternative stops recoils up to $T_C \approx 38$ MeV.

4.5.2 Operating modes over the Booster energy range

The stopping condition depends on both the beam energy and the recoil angle. Table 10 shows the recoil carbon range at Booster extraction ($T_p = 1.5$ GeV) across the detector angular acceptance, where the recoil energies are largest.

Table 8: Recoil ^{12}C laboratory angle θ_C corresponding to selected forward ^{3}He laboratory angles $\theta_{\rm fwd}$, for elastic ^{3}HeC scattering at four beam kinetic energies spanning the Booster acceleration ramp. All recoil angles fall within the recoil ring acceptance of 69.0°–91.3°, confirming kinematic coincidence coverage across the full ramp.

$\theta_{\rm fwd}$ (°)	$T = 6\,$MeV	$T = 450\,$MeV	$T = 1500\,$MeV	$T = 2496\,$MeV
		θ_C (°)		
7	85.6	85.5	85.2	84.8
9	84.4	84.2	83.8	83.4
11	83.1	82.9	82.4	81.9
13	81.9	81.6	81.0	80.5
15	80.6	80.3	79.7	79.0

Table 9: Electronic stopping power $-dE/dx$ and range of ^{12}C ions in silicon from SRIM-2013 [13], for kinetic energies spanning the recoil carbon range relevant for Booster polarimetry. A 300 µm thick Si detector stops ^{12}C up to $T_C = 38.0\,$MeV, and 500 µm up to $T_C \approx 59\,$MeV.

T_C (MeV)	$-dE/dx$ (MeV/µm)	Range (µm)
1	0.043	8
5	0.093	38
10	0.125	72
20	0.146	149
30	0.152	228
50	0.147	415
72	0.135	625
100	0.119	930
150	0.097	1520
197	0.083	2200

For pC scattering, the 500 µm detector operates in full-stopping mode over approximately 95% of the recoil angular acceptance ($\theta_C \gtrsim 72°$) throughout the Booster energy range. Only the innermost 3° of the acceptance ($\theta_C = 69°$–$72°$) transitions to ΔE mode at the highest Booster energies, where the recoil energy exceeds the stopping threshold. In this narrow angular band at extraction energy, the measured ΔE still provides a useful constraint in conjunction with the measured hit position, and the forward detector coincidence can be used as an additional cross-check.

For ^{3}He C scattering, the recoil carbon kinetic energy at extraction ($T_{^3\rm He} = 832\,$MeV/u) ranges from approximately 50 MeV at $\theta_C = 80°$ to 216 MeV at $\theta_C = 69°$, all of which exceed the 59 MeV stopping threshold. The detector therefore operates exclusively as a ΔE element for ^{3}He C scattering at extraction. The energy deposited in 500 µm of silicon spans approximately 42 MeV to 74 MeV over this angular range, providing a signal well above the noise threshold and sufficient for position and energy-loss determination. The elastic event identification in this regime relies on the forward coincidence constraint described in Sec. 4.4.2, which restores the full kinematic selectivity of the measurement.

At lower ^{3}He C beam energies (below approximately 100 MeV/u at injection), the recoil carbon energies fall below the stopping threshold and the detector returns to full-stopping mode, recovering the T_C–θ_C kinematic constraint. The transition between the two operating modes occurs smoothly during the Booster acceleration ramp and does not require any mechanical adjustment of the detector.

Table 10: Recoil ^{12}C kinetic energy T_C, forward proton scattering angle θ_p, and range in 500 µm silicon for elastic pC scattering at Booster extraction energy $T_p = 1.5\,\mathrm{GeV}$, as a function of recoil angle θ_C. The detector operates in full-stopping mode for $\theta_C \gtrsim 73°$ and as a ΔE element for the innermost strips at $\theta_C \approx 69°$ to $71°$.

θ_C (°)	θ_p (°)	T_C (MeV)	Range (µm)	Mode
69	35.0	78.7	695	ΔE
71	31.6	64.9	555	ΔE
73	28.2	52.3	437	stop
75	24.8	41.0	329	stop
80	16.5	18.4	137	stop
85	8.2	4.6	35	stop

4.6 Provision for deuteron polarimetry

The six-station azimuthal geometry of the polarimeter is suited in principle to measuring not only spin-$\frac{1}{2}$ beams (proton and ^{3}He) but also the spin-1 deuteron beam, for which the EIC program requires both vector and tensor polarization. The azimuthal yield distribution for elastic dC scattering on a transversely polarized beam takes the form

$$\frac{dN}{d\phi} \propto 1 + \tfrac{3}{2}\, A_y\, p_y \cos\phi + \tfrac{1}{2}\, A_{yy}\, p_{yy} \left(\cos^2\phi - \tfrac{1}{3}\right) + \ldots, \tag{42}$$

where p_y is the vector polarization, p_{yy} is the tensor polarization, A_y is the vector analyzing power, and A_{yy} is the tensor analyzing power. The $\cos\phi$ and $\cos 2\phi$ modulations are both well resolved by six equally spaced azimuthal stations, which provide unambiguous harmonic decomposition up to $n = 3$. The existing recoil ring therefore measures both p_y and p_{yy} without modification, provided A_y and A_{yy} are non-negligible in the angular range $\theta_C = 69°$–$91°$.

4.6.1 Kinematic comparison with ^{3}HeC scattering

At the maximum Booster rigidity $B\rho = 7.507\,\mathrm{T\,m}$ the deuteron ($m_d = 1875.613\,\mathrm{MeV/c^2}$, $q = +1$) reaches a kinetic energy of $T_d = 1054\,\mathrm{MeV}$ (527 MeV/u), with momentum $p_d = 2251\,\mathrm{MeV/c}$, equal to that of the proton at 1.5 GeV since both carry charge $q = +1$. Because the deuteron is lighter than ^{3}He, the forward-scattered deuteron is deflected to larger laboratory angles than ^{3}He for the same recoil carbon angle. Over the recoil detector acceptance $\theta_C = 69°$–$91°$, the forward deuteron angle spans $\theta_d \approx 2°$–$34°$, compared to $\theta_{^3\mathrm{He}} \approx 2°$–$28°$ for ^{3}He at the same recoil angles. The bulk of the useful acceptance, where the recoil carbon energy is sufficient for reliable detection ($T_C \gtrsim 10\,\mathrm{MeV}$, corresponding to $\theta_C \lesssim 82°$), maps to forward deuteron angles $\theta_d \approx 14°$–$34°$. This range lies entirely above the ^{3}He forward ring acceptance of 7.5°–14.8°, so the existing forward ring at $z = 750\,\mathrm{mm}$ provides no useful coincidence coverage for dC elastic scattering in the region of good recoil statistics.

4.6.2 Provision for a second forward ring

For deuteron polarimetry the forward coincidence serves two purposes. First, it provides the kinematic constraint needed to identify elastic dC events: the forward deuteron angle θ_d and the recoil carbon angle θ_C are uniquely related through the two-body kinematics, and requiring the measured pair (θ_d, θ_C) to lie on the elastic locus suppresses inelastic and quasi-elastic backgrounds. Second, it provides rejection of deuteron breakup events. The deuteron breaks up into $p + n$ with a separation energy of only 2.22 MeV, making breakup energetically accessible throughout the Booster range. In a breakup event the neutron escapes undetected, while the proton carries a large fraction of the beam momentum and may be emitted at a forward angle close to the elastic θ_d. Without a forward detector such events cannot be distinguished from elastic scattering on the basis of the recoil carbon signal alone, since the recoil carbon from a quasi-elastic pC collision within the deuteron can populate the same (θ_C, T_C) region as true elastic dC scattering. The forward coincidence rejects these events because the proton from breakup does not satisfy the dC elastic kinematic locus.

To accommodate future deuteron polarimetry the chamber design therefore includes blank flanges at $z = 400$ mm downstream of the target, at the azimuthal positions of the existing forward stations. At this longitudinal position the forward deuteron angles $\theta_d = 14°$–$34°$ correspond to radii $r = 100$–270 mm, as listed in Table 11. The inner edge at $r = 100$ mm matches the beam clearance of the existing rings. The radial extent of approximately 170 mm can be covered by two $98 \times 98\,\mathrm{mm}^2$ Hamamatsu silicon pads per station, the same detector type used in the ^{3}He forward ring. The dC ring at $z = 400$ mm is not expected to shadow the present ^{3}He forward ring at $z = 750$ mm: the ^{3}He ring subtends $\theta = 7.5°$–$14.8°$, which at $z = 400$ mm projects to $r = 53$–104 mm, i.e. largely within or very close to the beam-clearance region. The blank flanges are therefore not expected to affect the present ^{3}He forward-ring acceptance, although a detailed mechanical shadowing check is still required because the projected outer edge of the ^{3}He acceptance at $z = 400$ mm lies slightly beyond the nominal beam-clearance radius.

Table 11: Forward deuteron laboratory angle θ_d and corresponding detector radius r at $z = 400$ mm as a function of recoil carbon angle θ_C, for elastic dC scattering at the Booster extraction energy $T_d = 1054$ MeV ($B\rho = 7.507$ T m). The recoil carbon kinetic energy T_C is shown for reference.

θ_C (°)	θ_d (°)	r at $z = 400$ mm	T_C (MeV)
69	33.8	267	73.3
71	30.5	235	60.5
73	27.2	206	48.7
75	23.9	178	38.2
77	20.7	151	28.8
79	17.5	126	20.7
81	14.3	102	13.9
83	11.1	79	8.5
85	7.9	56	4.3

The availability of A_y and A_{yy} data for dC elastic scattering in the Booster energy range ($T_d \approx$ 200 MeV–1054 MeV) needs to be assessed before the performance of the deuteron polarimeter can be evaluated quantitatively. This is deferred to a future study.

4.7 Carbon target holder

The carbon target strip is held by a C-shaped rectangular support frame that approaches the interaction point from upstream ($z < 0$), entering the chamber at an angle with respect to the beam axis. The open end of the C-frame grips the ends of the target strip and positions it at the nominal beam interception point. The critical geometric constraint is that all components of the support structure remain at $z < 0$, so that neither the recoil carbon ejectiles traveling toward the recoil ring nor the forward-scattered projectiles traveling toward the forward ring are intercepted or shadowed by any part of the holder, as illustrated in Fig. 9.

The target holders are designed to allow transverse displacement of the strip in the xy plane with respect to the beam axis. By scanning the target transversely across the full beam cross section (beam sizes are listed in Table 12), different radial positions within the beam are sampled, opening the possibility to map the transverse polarization profile of the beam. Two holder orientations are foreseen, rotated by 60° about the beam axis relative to each other and consistent with the sixfold azimuthal symmetry of the detector stations, so that the polarization profile can be sampled along two independent transverse directions.

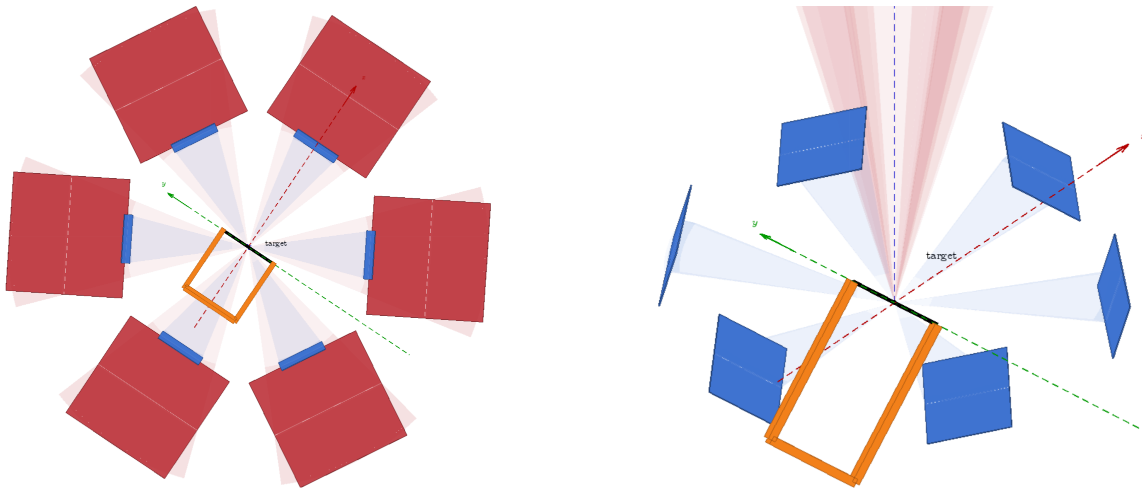

(a) View in beam (z) direction. (b) Target holder at beam interception $x = y = 0$.

Figure 9: Target holder with its support structure oriented such as to avoid obstruction of ejectiles paths to the forward or recoil detectors. All its components are at $z < 0$.

5 Polarization Measurement

5.1 Statistical figure of merit and target thickness

The statistical precision of a left-right asymmetry measurement is governed by the figure of merit defined in Eq. (11). For a circulating beam of N_{cyc} particles with revolution frequency f_{rev} traversing a carbon target of areal density d_t (g cm^{-2}), the required dwell time at a given beam energy to reach an absolute statistical precision δP on the polarization is obtained by inverting Eq. (24),

$$t_{\text{dwell}} = \frac{1}{N_{\text{cyc}}\, f_{\text{rev}}\, \dfrac{d_t N_A}{A_C}\, f_{\text{ov}}\, \Omega_{\text{eff}}\, \langle \text{FOM} \rangle\, (\delta P)^2}, \tag{43}$$

where $N_A = 6.022 \times 10^{23}\,\text{mol}^{-1}$ is Avogadro's number, $A_C = 12\,\text{g mol}^{-1}$ is the molar mass of carbon, Ω_{eff} is the effective accepted solid angle defined in Sec. 5.6.3, $\langle \text{FOM} \rangle$ is the corresponding acceptance-averaged figure of merit, and $f_{\text{ov}} \leq 1$ is the geometric overlap fraction between the beam cross section and the carbon target (Eq. (49), Table 12), as discussed in Sec. 5.2. A carbon target with areal density $d_t = 4\,\mu\text{g/cm}^2$ is assumed throughout, corresponding to

$$\frac{d_t N_A}{A_C} = 2.0 \times 10^{17}\,\text{cm}^{-2}. \tag{44}$$

This value follows the practice of the AGS pC polarimeter [24], where carbon strip targets of $3.7\,\mu\text{g/cm}^2$ to $4.5\,\mu\text{g/cm}^2$ have been used as internal beam targets without measurable degradation of stored beam lifetime. A dedicated residual-gas beam-loss analysis for the Booster confirms that the polarimeter vacuum section adds negligible loss for proton beams over the full acceleration ramp [25].

5.2 Geometric overlap of beam and carbon target

During heavy-ion Booster operation, the carbon-fiber target must be fully retracted and isolated from the polarimeter chamber behind a dedicated UHV gate valve: at the vacuum pressures required for heavy-ion running, any additional outgassing load from the target, its support structure, or associated hardware would compromise the chamber vacuum and increase residual-gas-induced beam loss [25]. The operational concept is therefore a clean separation of modes, the target remains parked and isolated during heavy-ion cycles, and is inserted into the beam line only for polarized light-ion running, for which the residual-gas loss constraints are far less stringent.

The carbon target is a thin strip produced by vacuum deposition of amorphous carbon. The CNI polarimeter targets developed for the AGS and RHIC [24, 26] have a measured areal density in the range $3.7\,\mu\mathrm{g/cm}^2$ to $4.5\,\mu\mathrm{g/cm}^2$, of which we adopt the nominal value

$$d_t = 4\,\mu\mathrm{g/cm}^2\,, \tag{45}$$

together with a strip width of $w = 10\,\mu\mathrm{m}$, established at RHIC (see Sec. 5.6 for further details regarding this choice). These vacuum-deposited films are markedly less dense than bulk carbon, a point worth emphasizing here: the measured areal density of $4\,\mu\mathrm{g/cm}^2$ is carried by a film only 25 nm to 30 nm thick, corresponding to an effective density of $\rho_{\mathrm{film}} \approx 1.4\,\mathrm{g/cm}^3$, well below the bulk amorphous-carbon value $\rho_C \approx 1.81\,\mathrm{g/cm}^3$ [27] and far below the graphite value $\rho_{\mathrm{graphite}} = 2.267\,\mathrm{g/cm}^3$ [28]. We therefore take d_t directly from the measured target characterization, rather than inferring it from a bulk density and an assumed geometric thickness, which would overestimate the areal density, and hence all interaction rates, by roughly a factor of two.

The interaction rate is governed by the amount of carbon the beam intersects, that is, by the cross-sectional area $A = w\,t$ of the strip, and is independent of the instantaneous strip orientation. As the strip rolls or twists about its long axis, the chord length traversed by a beam particle and the projected width $W_\perp(\psi)$ of the strip vary in opposite senses, but integrating the chord across the projected width sweeps the cross-section exactly once,

$$\int_{-W_\perp(\psi)/2}^{+W_\perp(\psi)/2} \ell_{\mathrm{chord}}(b,\psi)\,db = w\,t\,, \tag{46}$$

independently of the roll angle ψ. The rate is therefore the same in every orientation and may be evaluated in the face-on configuration, in which the column density along the beam is the measured areal density d_t, fixed by the thickness t, and the transverse overlap is set by the full width w.

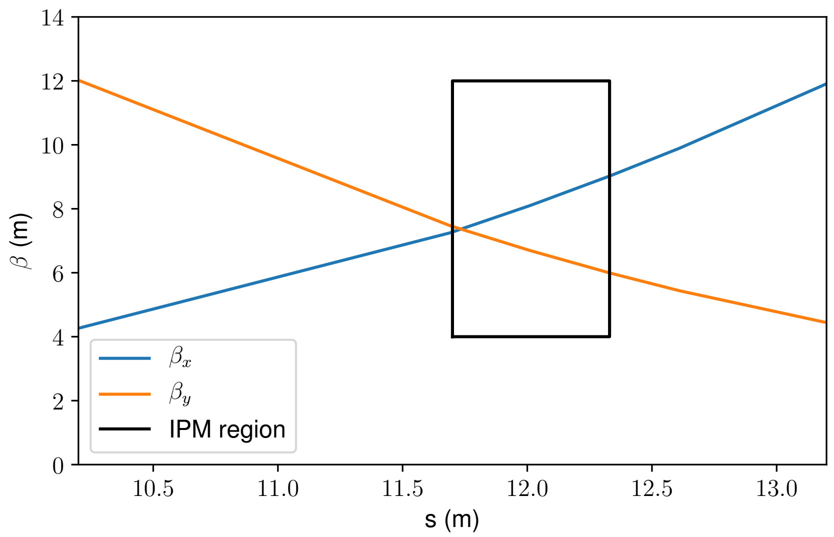

Figure 10: Beta functions β_x and β_y in the region where presently the Ionization Profile Monitor (IPM) of the Booster is installed, as a function of longitudinal position s. At the entrance of the IPM region ($s \approx 10.5\,\mathrm{m}$) both beta functions are approximately $\beta_x \approx \beta_y \approx 7.75\,\mathrm{m}$, indicating a round beam. (Figure taken from [29].)

The transverse beam size at the location of the Ionization Profile Monitor (IPM) is determined by the beta functions shown in Fig. 10 and the normalized emittance of the beam. For the polarized proton beam the normalized emittance is $\epsilon_N = 1\,\mu\text{m}$ [30], and since $\beta_x \approx \beta_y \approx 7.75\,\text{m}$ the beam is round at this location. The geometric emittance is related to the normalized emittance by

$$\epsilon_{\text{geo}} = \frac{\epsilon_N}{\beta\gamma}, \tag{47}$$

where $\beta\gamma$ is the Lorentz factor product at the given beam energy. The one-sigma beam radius is then

$$\sigma = \sqrt{\epsilon_{\text{geo}}\,\beta}, \tag{48}$$

where $\beta = 7.75\,\text{m}$ is the beta function at the target location. At Booster injection ($T_p = 200\,\text{MeV}$, $\beta\gamma = 0.69$) this gives $\sigma \approx 3.4\,\text{mm}$, and at extraction ($T_p = 1.5\,\text{GeV}$, $\beta\gamma = 2.40$) the beam has adiabatically cooled to $\sigma \approx 1.8\,\text{mm}$.

The carbon strip is narrow in x, of width w, and extends over the full beam height in y. For a beam with a two-dimensional Gaussian intensity distribution of widths σ_x and σ_y, the geometric overlap fraction is

$$f_{\text{ov}} = \underbrace{\int_{-w/2}^{+w/2} \frac{1}{\sqrt{2\pi}\,\sigma_x} e^{-x^2/2\sigma_x^2}\,dx}_{\text{narrow direction}} \cdot \underbrace{\int_{-\infty}^{\infty} \frac{1}{\sqrt{2\pi}\,\sigma_y} e^{-y^2/2\sigma_y^2}\,dy}_{=1}, \tag{49}$$

where the y integral is unity since the strip spans the full beam height. Using the identity

$$\int_{-a}^{+a} \frac{1}{\sqrt{2\pi}\,\sigma} e^{-x^2/2\sigma^2}\,dx = \text{erf}\left(\frac{a}{\sqrt{2}\,\sigma}\right), \tag{50}$$

with $a = w/2$, this reduces to

$$f_{\text{ov}} = \text{erf}\left(\frac{w}{2\sqrt{2}\,\sigma_x}\right) \approx \frac{w}{\sqrt{2\pi}\,\sigma_x}, \tag{51}$$

where the approximation holds for $w \ll \sigma_x$, well satisfied here ($w = 10\,\mu\text{m} \ll \sigma \approx 2\,\text{mm}$ to $5\,\text{mm}$). For a round beam $\sigma_x = \sigma_y = \sigma$, which is the case at the IPM location where $\beta_x \approx \beta_y$ (see Fig. 10). The resulting beam sizes, minimum target lengths, and overlap fractions are listed in Table 12.

Table 12: Beam size parameters and geometric overlap fraction f_{ov} at selected beam energies for the proton and ^{3}He beams. The beam sigma σ is computed from Eq. (48) using $\epsilon_N = 1\,\mu\text{m}$ and $\beta = 7.75\,\text{m}$ at the IPM location. The overlap fraction is evaluated using Eq. (51) with the strip width $w = 10\,\mu\text{m}$. The minimum required target length $L_{\text{min}} = 2 \times 5\sigma$ ensures coverage of the full $\pm 5\sigma$ beam envelope (see Sec. 5.3). The last ^{3}He row indicates the beam energy at which L_{min} reaches 50 mm.

Species	T (MeV)	$\beta\gamma$	σ (mm)	$L_{\text{min}} = 2 \times 5\sigma$ (mm)	f_{ov}
p	500	1.162	2.58	25.8	1.545×10^{-3}
p	850	1.623	2.19	21.9	1.825×10^{-3}
p	1200	2.048	1.95	19.5	2.051×10^{-3}
^{3}He	443	0.583	3.64	36.4	1.095×10^{-3}
^{3}He	132	0.310	5.00	50.0	0.798×10^{-3}

5.3 Required target length

The carbon strip must be long enough in the transverse direction to intercept the full beam envelope. Requiring coverage to $\pm 5\sigma$ encloses 99.9994% of the beam intensity and sets a minimum target length of $L_{\text{min}} = 2 \times 5\sigma$. From Table 12, the most demanding case is the ^{3}He beam at injection ($\sigma = 3.65\,\text{mm}$), giving $L_{\text{min}} = 36.5\,\text{mm}$. A target length of 50 mm, as used for the AGS CNI polarimeter [26], therefore provides adequate margin for both beam species across the full Booster acceleration cycle.

5.4 Polarimetry performance for pC elastic scattering

The beam parameters entering Eq. (43) for the proton beam are taken from Table 1: a single bunch of protons gives a total circulating intensity of $N_{\mathrm{cyc}} = 3.4 \times 10^{11}$ at a repetition frequency of 7.5 Hz. The revolution frequency rises from $f_{\mathrm{rev}} = 0.84$ MHz at injection to 1.37 MHz at extraction over a ramp time of $T_{\mathrm{ramp}} \approx 75$ ms. The relevant polarimetry channel is the recoil-ring singles mode, with the corresponding acceptance-averaged quantities defined in Sec. 5.6.3 and listed in Table 13.

The acceptance-averaged $\langle\mathrm{FOM}\rangle$ is computed from the Bonin parametrization [14] at three representative proton kinetic energies spanning the Booster ramp, as listed in Table 13. At 200 MeV the pC polarimeter behind the Linac already serves as an absolute reference point [31], so the Booster polarimeter is primarily relevant from about 300 MeV upward. Over the representative Booster energies considered here, the recoil-carbon acceptance is fully covered by the recoil ring (Tables 6 and 7), so the energy dependence of $\langle\mathrm{FOM}\rangle$ is driven by the underlying behavior of A_y and $d\sigma/d\Omega$, not by acceptance losses.

Figure 11 shows the dwell time t_{dwell} required to achieve an absolute statistical precision $\delta P = 1 \times 10^{-2}$, computed from Eq. (43). For the proton beam, the required dwell time remains within or comparable to the 75 ms ramp time over the representative Booster energy range considered here. The required statistical precision can therefore be reached within a single ramp cycle over essentially the full proton energy range relevant for Booster polarimetry.

5.4.1 Inelastic background in pC scattering

For pC polarimetry, inelastic background from ^{12}C excitation requires no special treatment. The low-lying excited states of ^{12}C that are kinematically accessible in the Booster energy range include the first excited state ($J^\pi = 2^+$) at $E_x = 4.44$ MeV, the Hoyle state ($J^\pi = 0^+$) at $E_x = 7.65$ MeV, and the $J^\pi = 3^-$ state at $E_x = 9.64$ MeV [32], where J^π denotes the spin and parity of the state. These states are excited in pC scattering and contribute to the inclusive forward proton yield. However, the Bonin parametrization of the differential yield $\varepsilon(\theta, e_c, p)$ [14] was obtained from measurements with thick carbon analyzer blocks and is explicitly inclusive; it parametrizes the total forward-scattered proton yield including contributions from elastic scattering and from excitation of these ^{12}C states. Similarly, the McNaughton parametrization of the analyzing power $A_y(\theta, p)$ [4] was derived from measurements that did not kinematically separate elastic from inelastic events. The two parametrizations are therefore internally consistent: the analyzing power applies to the inclusive yield that the Bonin parametrization describes, and no correction for inelastic contamination is required.

This inclusive nature of the pC parametrizations is in fact an advantage for the Booster polarimeter: the recoil ring operates in singles mode, detecting all recoil carbon nuclei within the kinematic acceptance without requiring an event-by-event elastic selection. The T_C–θ_C kinematic correlation provides a natural filter against non-carbon backgrounds (beam-gas scattering, secondary particles), but the separation of elastic from inelastic ^{12}C final states is not necessary for an unbiased polarization measurement with the Bonin and McNaughton parametrizations.

5.5 Polarimetry performance for ^{3}He C elastic scattering

For the ^{3}He beam the parameters from Table 1 are $N_{\mathrm{cyc}} = 1.0 \times 10^{11}$ (one bunch of $N_b = 1.0 \times 10^{11}$, current intensity) at a repetition frequency of 1 Hz and a ramp time of $T_{\mathrm{ramp}} \approx 75$ ms. The relevant polarimetry channel is the forward–recoil coincidence mode, with the corresponding acceptance-averaged quantities defined in Sec. 5.6.3 and listed in Table 13. The lower repetition rate of the EBIS source (1 Hz versus 7.5 Hz for protons, Table 1) reflects the pulse structure of the EBIS injector and enters directly into the wall-clock time required to accumulate a given number of ramp cycles.

The sole experimental anchor in the Booster energy range is the Kamiya et al. measurement at $T_{^3\mathrm{He}} = 443\,\mathrm{MeV}$ total kinetic energy [10]. The acceptance-averaged coincidence-channel quantities relevant for this case are listed in Table 13. The corresponding dwell time for $\delta P = 1 \times 10^{-2}$ is shown in Fig. 11.

The gap between the pC and ^{3}He C dwell times visible in Fig. 11 spans approximately three orders of magnitude. This follows from several factors acting in the same direction: the acceptance-averaged coincidence-channel quantities for ^{3}He C at 443 MeV are significantly smaller than the corresponding recoil-channel values for pC (Table 13); the geometric overlap factor f_{ov} is smaller for ^{3}He because of the larger beam size; and the lower beam intensity and lower revolution frequency of the ^{3}He beam further reduce the useful event rate. Together these effects account for the much longer dwell time required for ^{3}He polarimetry.

The dominant systematic uncertainty for ^{3}He C polarimetry is the calibration of A_y across the Booster energy range. As discussed in Sec. 6, the Kamiya measurement at 443 MeV is the only available anchor; no data exist above 450 MeV, and no reliable optical model extrapolation is available. The strategy for determining A_y in situ using the Booster polarimeter is discussed in Sec. 6.

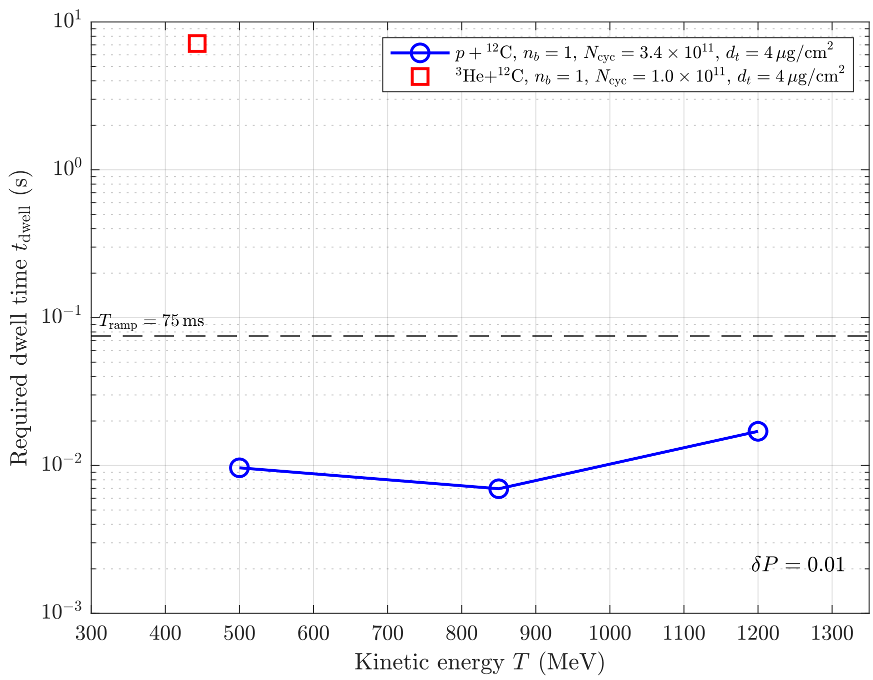

Figure 11: Required dwell time t_{dwell} to achieve an absolute statistical precision $\delta P = 1 \times 10^{-2}$ on the beam polarization, computed from Eq. (43), as a function of beam kinetic energy. Blue circles: p+^{12}C elastic scattering at three representative proton energies spanning the Booster ramp, using the recoil-channel quantities listed in Table 13. Red square: ^{3}He+^{12}C elastic scattering at $T_{^3\mathrm{He}} = 443\,\mathrm{MeV}$ [10], using the coincidence-channel quantities listed in Table 13. The dwell time is evaluated for the fully instrumented six-station detector system; since Table 13 lists rates per station, the rate entering Eq. (43) is $6 \times (R/\mathrm{stn})$. The dashed horizontal line marks the 75 ms ramp time. For protons, t_{dwell} is within or comparable to the ramp time depending on energy; for ^{3}He, accumulation over many ramp cycles is required at all energies.

5.5.1 Inelastic background for ^{3}He C elastic scattering

Two classes of background reactions must be controlled for ^{3}He C elastic polarimetry: excitation of the ^{12}C nucleus to low-lying inelastic states, and breakup of the ^{3}He projectile.

For ^{12}C excitation, the relevant states are the same as those listed in Sec. 5.4.1 for the pC case: the first excited state at 4.44 MeV, the Hoyle state at 7.65 MeV, and the state at 9.64 MeV [32]. In ^{3}He C scattering, excitation of these states shifts the recoil carbon angle θ_C to smaller values relative to the elastic locus at the same forward angle $\theta_{^3\mathrm{He}}$. This occurs because the heavier effective target mass $(M_C + E_x)$ reduces the transverse momentum transfer to the carbon nucleus at fixed forward angle, deflecting the recoil to a smaller polar angle. The shift is $\Delta\theta_C \lesssim -3^\circ$ within the forward detector acceptance and grows with increasing $\theta_{^3\mathrm{He}}$, as illustrated in Fig. 12.

For ^{3}He breakup, the two-body channel $^3\mathrm{He} \to p + d$ has a threshold of 5.49 MeV and is open throughout the Booster energy range. When the proton fragment scatters off ^{12}C, the lighter effective projectile mass results in less forward focusing of the recoil carbon, shifting θ_C to larger values relative to the elastic locus. The sign of the shift is opposite to that of ^{12}C excitation, so the two background classes appear on opposite sides of the elastic locus in the $(\theta_{^3\mathrm{He}}, \theta_C)$ plane. The three-body continuum $^3\mathrm{He} \to p + p + n$, with threshold at 7.72 MeV, populates a broad region bounded by the two-body $p + d$ envelope and is open throughout the Booster energy range. A full treatment of this three-body continuum would require a dedicated Monte Carlo simulation and is beyond the scope of the present analysis; the $p + d$ channel is used as a conservative estimate of the breakup background extent.

The forward detector provides two independent handles for background rejection. First, the kinematic constraint in the $(\theta_{^3\mathrm{He}}, \theta_C)$ plane places elastic events on a narrow locus that is well separated from both the inelastic and breakup populations, as shown in Fig. 12. With the detector segmentation and geometry adopted for the recoil and forward rings, the elastic locus is resolved from the 4.44 MeV inelastic state across the full acceptance. Second, the forward detector measures the energy deposit ΔE of the forward-scattered particle. In the 320 µm silicon forward detector, an intact $^3\mathrm{He}^{++}$ ion deposits of order 10 MeV, whereas a breakup proton deposits only of order 0.5 MeV. This large separation in ΔE, arising primarily from the Z^2 dependence of the Bethe–Bloch stopping power, provides particle identification independent of the kinematic-locus cut and cleanly rejects ^{3}He breakup events in which the forward particle is a proton rather than an intact helion.

5.6 Detector counting rates and operating modes

The width of the carbon strip is constrained by the rate capability of the recoil-ring readout rather than by target fabrication. The Timepix3 readout chip sustains a hit throughput of up to about 40 Mhits/s/cm^2 by design, with 20 Mhits/s/cm^2 demonstrated in first measurements [33]; beyond this the per-pixel dead time grows and the output bandwidth saturates. Because the counting rate scales linearly with the geometric overlap fraction, and therefore with the strip width w through Eq. (51), a wide strip would push the recoil ring into this regime: at the AGS strip widths of 75 µm to 250 µm the per-station recoil rate at the upper Booster energies would reach several tens of MHz, a chip-level throughput at or above the demonstrated Timepix3 value. We therefore adopt a narrow strip of width $w = 10$ µm, matching the carbon ribbons already in routine use in the RHIC CNI polarimeter [24]. At this width the per-station recoil rate ranges from about 3 to 10 MHz over the proton energy range (Table 13), with per-pixel occupancies below 10^{-4} and a maximum chip-level throughput of a few Mhits/s/cm^2, comfortably within the Timepix3 capability. The penalty in statistics is negligible: the required pC dwell time increases only to 7 ms to 17 ms, still well below the 75 ms Booster ramp time.

For pC polarimetry the dwell time established in Sec. 5.4 stays well within the 75 ms ramp duration over the representative energy range, so the required precision is reached within a single ramp cycle.

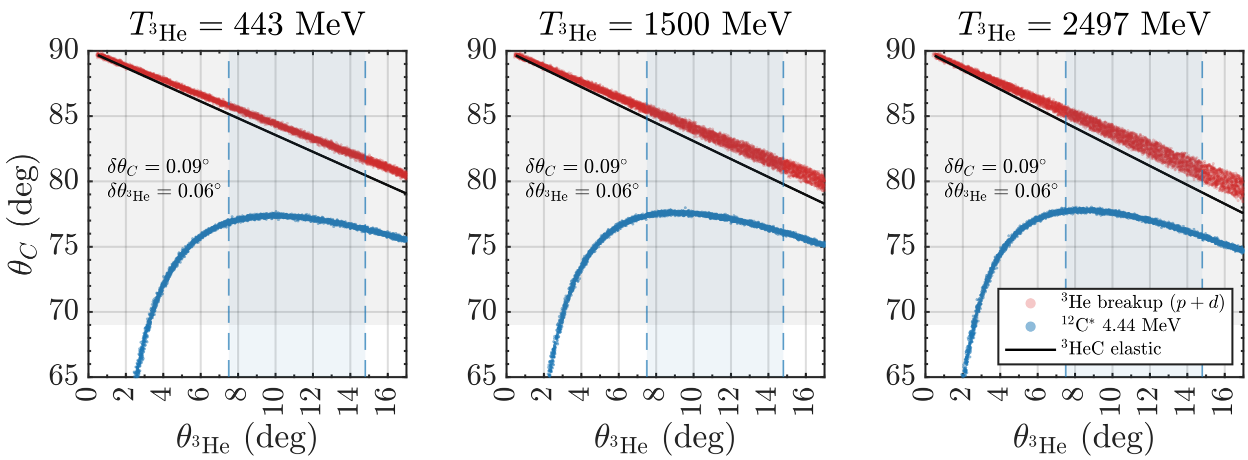

Figure 12: Kinematic separation of elastic $^3\mathrm{He} + {}^{12}\mathrm{C}$ scattering from inelastic backgrounds at three beam energies spanning the Booster acceleration cycle. Each panel shows the recoil carbon laboratory angle θ_C versus the forward ^{3}He laboratory angle $\theta_{^3\mathrm{He}}$ for elastic scattering (black line, infinite angular resolution), inelastic excitation of the first ^{12}C excited state at 4.44 MeV (blue points), and ^{3}He breakup via the $p + d$ channel (red points). The blue and red scatter points include realistic detector smearing ($\delta\theta_C = 0.09°$, $\delta\theta_{^3\mathrm{He}} = 0.06°$). The vertical blue band marks the forward detector acceptance ($\theta_{^3\mathrm{He}} = 7.5°$ to $14.8°$) and the horizontal grey band marks the recoil ring acceptance ($\theta_C = 69.0°$ to $91.3°$). Inelastic ^{12}C excitation shifts θ_C to smaller values (heavier effective recoil mass), while ^{3}He breakup shifts θ_C to larger values (lighter effective projectile mass), placing the two background classes on opposite sides of the elastic locus. A cut on the kinematic locus in the $(\theta_{^3\mathrm{He}}, \theta_C)$ plane, combined with ΔE identification of intact ^{3}He ions in the forward detector, is sufficient to isolate the elastic sample.

For ^{3}He C the dwell time greatly exceeds the ramp time and many cycles must be accumulated; the instantaneous rate is set by the coincidence acceptance and remains modest.

5.6.1 Target traversal and instantaneous rate

The instantaneous elastic scattering rate when the target ribbon is at transverse position x_0 relative to the beam center is

$$R(x_0) = N_{\mathrm{cyc}}\, f_{\mathrm{rev}}\, d_t\, f_{\mathrm{ov}}(x_0)\, \frac{d\sigma}{d\Omega}\, \Delta\Omega\,, \tag{52}$$

and is controlled by the transverse position of the ribbon through the overlap factor $f_{\mathrm{ov}}(x_0)$, which falls steeply as the target moves away from the beam center. Positioning the target off-axis is therefore a practical mechanism for rate reduction, at the cost of a proportionally longer dwell time for the same statistical precision. Moving the target faster through x_0, by contrast, reduces total counts without reducing the instantaneous rate while the ribbon is there, and is not a useful handle.

Reducing the circulating beam intensity N_{cyc} would also reduce the rate proportionally, but this option is excluded on physics grounds: the polarimeter must operate under the actual machine conditions to measure the polarization of the beam delivered to the AGS. Modifying N_{cyc}, the bunch filling pattern, or the RF parameters for the purpose of rate management would alter the very conditions under which the polarization is being measured, including space-charge tune shifts and depolarization resonance crossings. Off-axis target positioning is therefore the primary rate management tool available.

5.6.2 Strip segmentation and per-strip occupancy

The forward ring sensors are strip devices carrying 128 radial strips per station, subdividing the radial extent $r = 100$ to $198\,\text{mm}$ into $\Delta r \approx 0.77\,\text{mm}$ per strip. For the recoil ring, a pixel detector such as Timepix3 [33] is under consideration; the segmentation and occupancy per pixel then depend on the chip geometry and assembly, and are discussed in Sec. 5.6.3. In either case the relevant figure for pile-up is the occupancy per sensitive element per shaping window,

$$\mathcal{O} = R_{\text{strip}} \times \tau_{\text{shape}}\,, \tag{53}$$

where $R_{\text{strip}} = R_{\text{stn}}/N_{\text{seg}}$, N_{seg} is the number of independent sensitive elements per station, and τ_{shape} is the detector shaping time. As shown in Table 13, the resulting occupancies are negligible for all operating modes at beam center, with values well below 10^{-5} per sensitive element at 100 ns shaping time.

5.6.3 Counting rate summary

Table 13 summarises the acceptance-averaged differential cross section $\langle d\sigma/d\Omega\rangle$, the acceptance-averaged $\langle\text{FOM}\rangle$, and the resulting counting rates per station for all operating modes and beam species. For a given detector mode, let $\chi(\theta,\phi)$ denote the acceptance function, with $\chi(\theta,\phi) = 1$ if an event at (θ,ϕ) is accepted and $\chi(\theta,\phi) = 0$ otherwise. The acceptance-averaged quantities are then defined by

$$\left\langle \frac{d\sigma}{d\Omega} \right\rangle = \frac{\displaystyle\int \chi(\theta,\phi)\,\frac{d\sigma}{d\Omega}(\theta)\,d\Omega}{\displaystyle\int \chi(\theta,\phi)\,d\Omega}, \qquad \langle\text{FOM}\rangle = \frac{\displaystyle\int \chi(\theta,\phi)\,A_y^2(\theta)\,\frac{d\sigma}{d\Omega}(\theta)\,d\Omega}{\displaystyle\int \chi(\theta,\phi)\,d\Omega}, \tag{54}$$

with

$$\Omega_{\text{eff}} = \int \chi(\theta,\phi)\,d\Omega, \qquad d\Omega = \sin\theta\,d\theta\,d\phi\,.^{1} \tag{55}$$

Because the six stations of a given ring are geometrically identical and the elastic observables are azimuthally symmetric, the acceptance-averaged quantities $\langle d\sigma/d\Omega\rangle$ and $\langle\text{FOM}\rangle$ are numerically the same whether evaluated for one station or for the full six-station ring; only the effective accepted solid angle Ω_{eff}, and hence the total rate, scales with the number of stations.

For elastic pC and ^{3}He C scattering, neither $d\sigma/d\Omega$ nor A_y depends on the azimuthal angle ϕ; the ϕ dependence enters only through the acceptance function $\chi(\theta,\phi)$. For pC, the observables are calculated from the Bonin parametrization [14]; for ^{3}He C at 443 MeV, they are obtained from the digitized Kamiya *et al.* data converted to the laboratory frame [10]. Beam parameters are taken from Table 1, and the beam–target geometric overlap factor f_{ov} is evaluated from Eq. (51) using the strip width $w = 10\,\mu\text{m}$ and the nominal beam σ at each energy.

Several conclusions follow from Table 13.

For pC, the singles rates and occupancies listed in Table 13 are comfortably low, confirming that pile-up is not a concern for recoil-ring singles operation at beam center. The recoil detector can therefore operate in data-driven single-hit mode without rate-related limitations under nominal beam conditions.

For ^{3}He C, both the recoil-ring singles rate and the forward-ring coincidence rate remain low, with negligible occupancies in either case (Table 13). The design driver for the ^{3}He C mode is therefore threshold and efficiency for single-hit detection, not rate capability.

[1] For a sphere parametrized by $\vec{r}(\theta,\phi) = r(\sin\theta\cos\phi, \sin\theta\sin\phi, \cos\theta)$, the surface element is $dA = |\partial\vec{r}/\partial\theta \times \partial\vec{r}/\partial\phi|\;d\theta\,d\phi = r^2\sin\theta\,d\theta\,d\phi$, hence $d\Omega = dA/r^2 = \sin\theta\,d\theta\,d\phi$.

Table 13: Acceptance-averaged differential cross sections, acceptance-averaged ⟨FOM⟩, counting rates, and detector occupancies for pC (singles mode, recoil ring) and ^{3}He C (singles and coincidence modes) at representative Booster energies. The acceptance-averaged quantities are defined in Eqs. (54) and (55). The geometric overlap factor $f_{\rm ov}$ is evaluated from Eq. (51) using the strip width $w = 10\,\mu$m and the nominal beam σ from Table 12. Geometric parameters and per-station solid angles are given in Table 6. Rates are quoted per detector station (6 stations per ring). The occupancy $\mathcal{O}_{\rm det}$ is the fractional dead time per sensitive element: for pC singles and ^{3}He C singles in the recoil ring, a Timepix3 detector with 475 ns per-pixel dead time and 256×256 pixels per chip is assumed [33]; for ^{3}He C coincidence in the forward ring, a strip ASIC with 100 ns shaping time and 128 strips per station is assumed. For pC, the acceptance-averaged observables are calculated from the Bonin parametrization [14]; for ^{3}He C at 443 MeV, they are obtained from digitized Kamiya *et al.* data converted to the laboratory frame [10]. For azimuthally symmetric elastic scattering, the quoted $\langle d\sigma/d\Omega\rangle$ and ⟨FOM⟩ are numerically identical whether evaluated for one station or for the full six-station ring.

Species	Mode	T (MeV)	$f_{\rm ov}$	$\langle d\sigma/d\Omega\rangle$ (mb/sr)	⟨FOM⟩ (mb/sr)	R/stn	$\mathcal{O}_{\rm det}$
pC	singles	500	1.545×10^{-3}	378.80	20.18	3.24 MHz	2.35×10^{-5}
		850	1.825×10^{-3}	584.78	21.04	6.65 MHz	4.82×10^{-5}
		1200	2.051×10^{-3}	770.17	7.24	10.41 MHz	7.54×10^{-5}
^{3}He C	singles	443	1.095×10^{-3}	297.19	9.81	123.79 kHz	8.97×10^{-7}
^{3}He C	coinc.	443	1.095×10^{-3}	17.15	1.44	2.78 kHz	2.17×10^{-6}

The Booster RF structure introduces an additional consideration: the rates in Table 13 are averaged over the full revolution period. With harmonic number $h = 3$ and a single filled bunch, the beam occupies approximately one-third of each revolution period, so the instantaneous rate during the bunch passage is roughly three times higher than the cycle-averaged values. Even with this correction, the per-pixel occupancies remain below 10^{-5} and pile-up is not a concern.

5.6.4 Operating modes

For pC polarimetry the standard operating mode is singles mode: elastic recoil carbon is detected in the recoil ring without a coincidence requirement. The corresponding recoil-ring geometric acceptance is summarized in Table 6. As discussed in Sec. 5.4.1, the Bonin parametrization is inclusive and already accounts for contributions from elastic and inelastic ^{12}C excitation; a forward coincidence requirement therefore provides no additional physics discrimination for pC and is not needed. The forward ring may nonetheless be operated in parallel as a monitor and cross-check of the recoil ring measurement. As shown in Fig. 4, the forward-ring acceptance overlaps the region of largest figure of merit at intermediate proton energies and samples the falling high-angle shoulder of the distribution at the highest representative energy considered here. In both cases the recoil detector sees the full singles rate of Table 13; operating the forward ring in monitor mode does not reduce the instantaneous load on the recoil detector.

For ^{3}He C polarimetry the forward coincidence is not optional: it is required to suppress ^{3}He breakup events, which would otherwise contaminate the elastic sample and bias the asymmetry measurement (Sec. 4.1.2). The ^{3}He C rate is therefore always that of the coincidence mode, with the recoil ring providing the singles rate as an independent cross-check.

6 Light-ion polarimetry at Booster energies: uncharted territory

The use of ^{3}He+C elastic scattering as a polarimeter requires knowledge of the analyzing power A_y across the full Booster energy range. As established in Sec. 3.3 and Fig. 5, the sole experimental anchor point is the measurement by Kamiya *et al.* at 443 MeV [10], which yielded A_y reaching 0.63 near $\theta_{\text{lab}} \approx 6°$–$7°$ with the figure-of-merit peak falling within the forward detector acceptance as discussed in Sec. 4.3. Above 450 MeV, no ^{3}He+C analyzing power data exist anywhere in the literature, and no calibrated optical model parametrization extends into this regime. The following subsections discuss the expected behavior of A_y in this uncharted range and the strategy for determining it experimentally using the Booster polarimeter itself.

6.1 Missing data, theoretical expectations, and kinematic constraints

Global optical potential parametrizations for ^{3}He projectiles, including those of Trost *et al.* [34] and Pang *et al.* [35], are calibrated to energies below 220 MeV and 250 MeV respectively, and cannot be extrapolated reliably into the Booster range. The optical model fit reported in Ref. [10] parametrizes the spin-orbit interaction through a Woods-Saxon derivative form factor whose surface thickness is characterized by a diffuseness parameter a_{SO}: a small value implies a sharp, surface-confined spin-orbit force, while a large value implies a spatially extended interaction. The fit at 443 MeV yielded $a_{\text{SO}} = 0.6$–0.8 fm, in contrast to the much smaller values of 0.2–0.3 fm found in optical model analyses at lower energies, indicating that the spin-orbit interaction evolves significantly with energy already below 500 MeV. The behavior of A_y throughout most of the Booster acceleration ramp is therefore unknown both experimentally and theoretically.

Some qualitative guidance follows from the better-studied p+C system. The Bonin parametrization, [4,14] describes the smooth exponential forward peak of the p+C differential cross section and shows that A_y remains in the range 0.1 to 0.3, with a relatively weak momentum dependence of the figure of merit over the range 1.0 to 2.0 GeV/c. For ^{3}He+C the situation differs in three important respects. First, the larger effective interaction radius leads, within standard optical-model systematics [36,37], to a narrower diffraction peak, shifting the useful angular range to smaller laboratory angles. This is consistent with the forward location of the A_y maximum near $6°$–$7°$ at 443 MeV. Second, the analyzing power originates predominantly from the spin–orbit interaction and can be related, in the impulse approximation, to the underlying nucleon–nucleon amplitudes [37,38], providing a physical basis for a non-vanishing A_y at higher energies. Third, by analogy with α+C elastic scattering, [37], the differential cross section becomes increasingly forward-peaked with energy, concentrating the figure of merit near the forward maximum.

A further kinematic concern is the migration of the figure-of-merit peak toward smaller laboratory angles with increasing beam momentum. Since the forward scattering peak in the CM frame scales approximately as $1/p_{\text{CM}}$, the laboratory angle of peak A_y shifts from $6°$–$7°$ at 443 MeV toward approximately $3°$–$4°$ at Booster extraction energy, well inside the inner edge of the forward detector acceptance at $7.5°$ (Fig. 6). This migration motivates the far-forward detector ring discussed in the Conclusion, and must be taken into account in any evaluation of the effective figure of merit integrated over the forward detector acceptance at the highest Booster energies.

6.2 Determining A_y in the presence of depolarization resonances

During acceleration in the Booster the ^{3}He beam traverses a series of spin-depolarizing resonances as the spin tune $\nu_s = G\gamma$ sweeps from -4.193 at injection through -4.5 after bunch merging (Table 1, note a) to -7.904 at extraction. Simulations and resonance analysis presented by Hock [29] show that three imperfection resonances are crossed up to $|G\gamma| = 7.5$ and two intrinsic resonances are encountered up to $|G\gamma| = 10.5$. Resonance crossing is managed through harmonic orbit correction and AC dipole techniques. Full spin-flip has been demonstrated in simulation at the intrinsic resonances $|G\gamma| = 12 - \nu_y$ and $6 + \nu_y$ with AC dipole integrated strengths of $1.65\,\mathrm{mT\cdot m}$ and $2.05\,\mathrm{mT\cdot m}$ respectively [29]. Nevertheless, partial depolarization at individual resonances cannot be excluded, particularly where the required corrector currents approach the supply limits.

Determining A_y at an energy where it is unknown requires the beam polarization at that energy, which the intervening resonances render uncertain. The polarimeter resolves this by exporting the absolute polarization scale from the single reference energy of 443 MeV, where the ^{3}He+C analyzing power is known from Kamiya *et al.* [10], to any other energy in the ramp through a ramp-and-return calibration. In its elementary form, the beam is prepared at the reference energy $A = 443\,\mathrm{MeV}$ with known polarization P_A, ramped to the target energy B where the scattering asymmetry is measured, and returned to A where the polarization P'_A is measured a second time, so that the round-trip loss $\Delta P = P_A - P'_A$ is obtained directly. Since depolarization cannot increase the polarization on either leg of the excursion, the polarization at B is bracketed by the two measurements, $P'_A \leq P_B \leq P_A$, independently of how the loss is distributed between the up- and down-ramps. The midpoint $\widehat{P}_B = \frac{1}{2}(P_A + P'_A)$ is the estimate of P_B with the smallest worst-case error, $\Delta P/2$, and $A_y(B)$ then follows from the measured asymmetry as $\varepsilon_B/\widehat{P}_B$.

Rather than bridging the full range in a single excursion, the scale is propagated by a ladder of short, adjacent round-trips, $A \to B \to A$, $B \to C \to B$, $C \to D \to C$, and so on, anchored at $A = 443\,\mathrm{MeV}$ and extending both upward toward extraction and downward as an independent chain. Each rung rests only on the polarizations measured at its own two endpoints and on its own round-trip loss. With only a few resonances spread across the ramp, most rungs cross none and return a ΔP consistent with zero, while the few that straddle a resonance isolate a single one and carry the loss; each rung is thereby self-validating, an anomalous crossing appears as a large local ΔP and implicates only that rung. Steps of order 100 MeV ensure that no rung contains more than one resonance. Because the calibration is chained, the uncertainty on the absolute polarization accumulates along the ladder. With each rung verified to keep, for instance, $\Delta P \leq 0.01$ and estimated by its midpoint, the per-rung errors are independent and add in quadrature, so that after n rungs the accumulated uncertainty is $\sigma_n \approx (\Delta P/2)\sqrt{n}$. Reaching extraction at $T \approx 2.5\,\mathrm{GeV}$ ($\gamma \approx 1.89$, $\nu_s = G\gamma = -7.904$) from the 443 MeV anchor requires $n \approx 20$ steps, giving a conservative $\sigma_{\mathrm{ext}} \approx \sqrt{20} \times 0.005 \approx 0.022$ in absolute polarization, of order 2% absolute and 4% relative for an extraction polarization near 0.5. Since most rungs cross no resonance, this bound charges every step the full ΔP when the loss is in practice carried by the few resonance-crossing rungs; how small a ΔP can be enforced at each step, and hence the precision ultimately reached, depends mostly on the beam time invested in the calibration.

The quadrature scaling relies on the per-rung brackets being free of a common bias. This holds because the depolarizing resonances sit at fixed $G\gamma$ and are not aligned with the chosen rung boundaries, so the residual offsets between $\widehat{P}$ and the true polarization carry no common sign; a directional bias would instead accumulate linearly, $\sigma_n \leq (\Delta P/2)\,n$, which bounds the worst case. Repeating the ladder with deliberately irregular step sizes slices the same fixed resonances into different rungs, averaging down any residual bias and providing a direct diagnostic at the energies where the partitions disagree. This calibration by excursion has been demonstrated at the IUCF Cooler Ring [39], where it was used to export the polarization scale for *pp* elastic analyzing-power and spin-correlation measurements from 200 MeV to 450 MeV [40]. Applied to the Booster, it makes the recoil-carbon polarimeter a practical instrument for the systematic determination of ^{3}He+C analyzing powers across the full acceleration ramp.

The primary motivation is not the measurement of these data in isolation, but their use in optimizing polarization transmission through the accelerator chain: knowledge of A_y at each stage of the ramp allows resonance crossing conditions to be tuned to minimize polarization loss, and the same strategy extends naturally beyond the Booster to the AGS, where the carbon-recoil polarimeter provides the analogous absolute reference at higher energies.

6.3 Outlook for deuteron and lithium polarimetry

The recoil-carbon detector geometry described in this paper applies without modification to deuteron, ^{6}Li, and ^{7}Li beams, since the kinematic arguments of Sec. 2 depend only on the projectile-to-carbon mass ratio and the magnetic rigidity.

For the deuteron the spin dynamics during Booster acceleration are uniquely favorable. With $G_d = -0.1426$ (Table 5), the spin tune $\nu_s = G_d\gamma$ remains well below unity throughout the full acceleration cycle, so neither imperfection nor intrinsic depolarizing resonances are crossed [18]. The analyzing power data situation is correspondingly well developed: Satou et al. [19] measured A_y and A_{yy} at 270 MeV, Müller et al. [20] extended the world data set with A_y measurements at seven energies between 170 and 380 MeV at COSY, and the same group demonstrated efficient dC polarimetry at $p = 0.97$ GeV/c [21], approaching Booster extraction momentum. The experimental basis for dC polarimetry across the full Booster energy range is therefore comparable in quality to the pC case. The forward deuteron angles $\theta_d = 14°$–$34°$ lie entirely above the existing ^{3}He forward ring acceptance, and blank flanges are provisioned at $z = 400$ mm for a future deuteron forward ring as described in Sec. 4.6.2.

For ^{6}Li, $G_{^6\mathrm{Li}} = -0.178$ is close to the deuteron value, and the spin dynamics during Booster acceleration are similarly favorable with few depolarizing resonances. For ^{7}Li, $G_{^7\mathrm{Li}} = +1.532$ is close to the proton value $G_p = +1.793$, and polarized ^{7}Li acceleration faces a resonance density comparable to that of the proton, requiring analogous mitigation strategies. In neither case do A_y data exist in the Booster energy range: ^{6}Li vector analyzing power measurements on ^{12}C extend only to 150 MeV [22], and for ^{7}Li only unpolarized differential cross sections have been measured at intermediate energies [23]. The Booster polarimeter is therefore identified as the instrument to map the LiC analyzing power across the full acceleration range, in direct analogy to the role foreseen for ^{3}HeC polarimetry in Sec. 6.

7 Conclusion

A recoil-carbon polarimeter concept has been developed for the BNL Booster synchrotron to measure the transverse polarization of both the polarized proton beam and the polarized ^{3}He ion beam throughout the acceleration cycle. The polarimeter consists of coaxial recoil and forward silicon detector rings with six shared azimuthal stations, as summarized in Table 6. The detector geometry provides continuous kinematic coverage for proton and ^{3}He polarimetry over the Booster ramp. The design is staged for commissioning: Stage 1 instruments only the recoil ring, which is sufficient for pC polarimetry with event identification based on the recoil kinematics alone; Stage 2 adds the forward ring, enabling ^{3}He C polarimetry through the forward-coincidence condition together with ΔE identification, which suppresses both ^{3}He breakup backgrounds and inelastic ^{12}C excitation. The two stages are mechanically independent and can be commissioned sequentially, allowing proton polarimetry to proceed while the forward ring is being prepared.

For pC elastic scattering, analyzing-power and differential-cross-section data from multiple experiments across the Booster energy range establish a well-characterized figure of merit in the recoil acceptance. The corresponding acceptance-averaged quantities and dwell times are summarized in Table 13 and Fig. 11. Over the representative proton energies considered here, the dwell time required to reach an absolute statistical precision $\delta P = 1 \times 10^{-2}$ remains within or comparable to the 75 ms ramp time. Proton polarimetry in the Booster is therefore statistically feasible within a single ramp cycle over essentially the full relevant energy range, so that the total uncertainty budget is expected to be dominated by systematic effects from the outset.

For ^{3}He C elastic scattering, the sole experimental anchor in the Booster energy range is the Kamiya et al. measurement at 443 MeV [10]. The corresponding acceptance-averaged quantities and dwell time are summarized in Table 13 and Fig. 11. In contrast to the proton case, the dwell time required to reach an absolute statistical precision $\delta P = 1 \times 10^{-2}$ greatly exceeds the 75 ms ramp time, so ^{3}He polarimetry necessarily requires accumulation over many ramp cycles.

As the ^{3}He beam energy increases along the ramp, the forward-angle structure of the ^{3}He C elastic-scattering observables shifts to smaller laboratory angles. At the 443 MeV Kamiya anchor energy, the present forward ring samples the useful forward-angle region relevant for polarimetry. At higher ^{3}He energies, however, the most favorable angular region moves closer to the beam. The chamber design already includes additional flanges that could support an extension into this region, so the basic mechanical provision is in place. The present $98 \times 98\,\text{mm}^2$ pad detectors cannot be used for this purpose, since their azimuthal extent would cause adjacent stations to overlap if the inner active edge were moved substantially inward. An extension toward smaller forward angles would therefore require only the corresponding detector instrumentation with smaller sensors and an optimized layout.

The chamber design includes blank flanges at $z = 400$ mm at the azimuthal positions of the existing forward stations, providing a mechanical provision for future deuteron polarimetry without affecting current operation. At the maximum Booster rigidity $B\rho = 7.507$ T m the elastic dC kinematic locus maps the recoil acceptance $\theta_C = 69°–82°$ to forward deuteron angles $\theta_d = 14°–34°$, a range entirely above the existing ^{3}He forward ring acceptance and covered by populating these flanges with silicon detectors. With six azimuthal stations, both the $\cos\phi$ and $\cos 2\phi$ modulations of the dC yield are resolved, enabling simultaneous measurement of vector and tensor polarization should a deuteron program at EIC be pursued in the future.

The Booster polarimeter provides an operationally independent polarimetry capability at a time when the AGS is undergoing an extended refurbishment, including a major recabling effort. With the AGS pC polarimeter unavailable during this period, the Booster instrument allows polarimetry development, A_y calibration campaigns, and spin-resonance studies to proceed for both the proton and ^{3}He programs. More generally, the continuous polarization monitoring it provides throughout the Booster ramp is directly relevant to optimizing polarization transmission into the AGS and, ultimately, into the EIC hadron storage ring.

Acknowledgments

The authors thank M. Minty for a careful reading of the manuscript and for several valuable comments. This work was supported by Brookhaven Science Associates, LLC under Contract No. DE-SC0012704 with the U.S. Department of Energy.

References

[1] W. T. Weng, L. Ahrens, R. Damm, and A. J. McNerney. Construction and early commissioning results of the AGS booster. In *Proc. PAC'91*, pages 52–54, 1991. URL: https://proceedings.jacow.org/p91/PDF/PAC1991_0052.PDF.

[2] J. Alessi et al. Performance of the new EBIS preinjector. In *Proc. PAC'11*, 2011. BNL-94248-2011-CP. URL: https://www.bnl.gov/isd/documents/75603.pdf.

[3] R.D. Ransome, C.L. Hollas, P.J. Riley, B.E. Bonner, W.D. Cornelius, O.B. van Dyck, E.W. Hoffman, M.W. McNaughton, R.L. York, S.A. Wood, and K. Toshioka. Measurement of the p-c analyzing power between 100 and 750 mev and the p-be analyzing power at 780 mev. *Nuclear Instruments and Methods in Physics Research*, 201(2):315–321, 1982. URL: https://www.sciencedirect.com/science/article/pii/0167508782905580, doi:10.1016/0167-5087(82)90558-0.

[4] M.W. McNaughton, B.E. Bonner, H. Ohnuma, O.B. Van Dijk, Sun Tsu-Hsun, C.L. Hollas, D.J. Cremans, K.H. McNaughton, P.J. Riley, R.F. Rodebaugh, Shen-Wu Xu, S.E. Turpin, B. Aas, and G.S. Weston. The p-c analyzing power between 100 and 750 mev. *Nuclear Instruments and Methods in Physics Research Section A: Accelerators, Spectrometers, Detectors and Associated Equipment*, 241(2):435–440, 1985. URL: https://www.sciencedirect.com/science/article/pii/0168900285905959, doi:10.1016/0168-9002(85)90595-9.

[5] Hans-Otto Meyer. The Indiana Cooler: A retrospective. *Annu. Rev. Nucl. Part. Sci.*, 57:1–34, 2007. doi:10.1146/annurev.nucl.57.090506.123124.

[6] C. Wilkin et al. The legacy of the experimental hadron physics programme at COSY. *Eur. Phys. J. A*, 53:114, 2017. doi:10.1140/epja/i2017-12295-4.

[7] N. H. Buttimore et al. Spin dependence of high energy proton scattering. *Phys. Rev. D*, 59:114010, 1999. doi:10.1103/PhysRevD.59.114010.

[8] I. G. Alekseev et al. The AGS CNI polarimeter. In *Proc. 15th Int. Spin Physics Symp. (SPIN 2002)*, volume 675 of *AIP Conf. Proc.*, pages 803–807. AIP, 2003. doi:10.1063/1.1607256.

[9] H. Huang and K. Kurita. Fiddling carbon strings with polarized proton beams. *AIP Conf. Proc.*, 868:3–21, 2006. doi:10.1063/1.2401392.

[10] J. Kamiya, K. Hatanaka, T. Adachi, K. Fujita, K. Hara, T. Kawabata, T. Noro, H. Sakaguchi, N. Sakamoto, Y. Sakemi, Y. Shimbara, Y. Shimizu, S. Terashima, M. Uchida, T. Wakasa, Y. Yasuda, H. P. Yoshida, and M. Yosoi. Cross section and induced polarization in ^{3}He elastic scattering at 443 mev. *Phys. Rev. C*, 67:064612, Jun 2003. URL: https://link.aps.org/doi/10.1103/PhysRevC.67.064612, doi:10.1103/PhysRevC.67.064612.

[11] E. Tiesinga, P. J. Mohr, D. B. Newell, and B. N. Taylor. Codata recommended values of the fundamental physical constants: 2018. *Rev. Mod. Phys.*, 93:025010, 2021. URL: https://link.aps.org/doi/10.1103/RevModPhys.93.025010, doi:10.1103/RevModPhys.93.025010.

[12] Eero Byckling and Kustaa Kajantie. *Particle Kinematics*. John Wiley & Sons, London, 1973.

[13] James F. Ziegler, M. D. Ziegler, and J. P. Biersack. SRIM – the stopping and range of ions in matter (2010). *Nucl. Instrum. Meth. B*, 268:1818–1823, 2010. doi:10.1016/j.nimb.2010.02.091.

[14] B. Bonin et al. Measurement of the Inclusive p C Analyzing Power and Cross-section in the 1-GeV Region and Calibration of the New Polarimeter Pomme. *Nucl. Instrum. Meth. A*, 288:379, 1990. doi:10.1016/0168-9002(90)90128-S.

[15] G. W. Hoffmann et al. Polarized proton elastic scattering from polarized C-13. *Phys. Rev. Lett.*, 65:3096–3099, 1990. URL: https://link.aps.org/doi/10.1103/PhysRevLett.65.3096, doi:10.1103/PhysRevLett.65.3096.

[16] M. Wang et al. The AME 2020 atomic mass evaluation. *Chinese Physics C*, 45(3):030003, 2021. doi:10.1088/1674-1137/abddaf.

[17] N.J. Stone. Table of nuclear magnetic dipole and electric quadrupole moments. *Atomic Data and Nuclear Data Tables*, 90(1):75–176, 2005. URL: https://www.sciencedirect.com/science/article/pii/S0092640X05000239, doi:10.1016/j.adt.2005.04.001.

[18] S. Y. Lee. *Spin Dynamics and Snakes in Synchrotrons*. World Scientific, Singapore, 1997. doi:10.1142/3233.

[19] Y Satou, S Ishida, H Sakai, H Okamura, N Sakamoto, H Otsu, T Uesaka, A Tamii, T Wakasa, T Ohnishi, K Sekiguchi, K Yako, K Suda, M Hatano, H Kato, Y Maeda, J Nishikawa, T Ichihara, T Niizeki, H Kamada, W Glöckle, and H Witała. Three-body dn interaction in the analysis of the ^{12}c(d, d') reaction at 270 mev. *Physics Letters B*, 549(3):307–313, 2002. URL: https://www.sciencedirect.com/science/article/pii/S037026930202957X, doi:10.1016/S0370-2693(02)02957-X.

[20] F. Müller, M. Żurek, Z. Bagdasarian, L. Barion, M. Berz, I. Ciepal, G. Ciullo, S. Dymov, D. Eversmann, M. Gaisser, R. Gebel, K. Grigoryev, D. Grzonka, V. Hejny, N. Hempelmann, J. Hetzel, F. Hinder, A. Kacharava, V. Kamerdzhiev, I. Keshelashvili, I. Koop, A. Kulikov, A. Lehrach, P. Lenisa, N. Lomidze, B. Lorentz, P. Maanen, G. Macharashvili, A. Magiera, D. Mchedlishvili, A. Nass, N. N. Nikolaev, A. Pesce, D. Prasuhn, J. Pretz, F. Rathmann, V. Rolando, M. Rosenthal, A. Saleev, V. Schmidt, Y. Senichev, D. Shergelashvili, V. Shmakova, A. Silenko, J. Slim, H. Soltner, A. Stahl, R. Stassen, E. Stephenson, H. Ströher, M. Tabidze, G. Tagliente, R. Talman, F. Trinkel, Yu. Uzikov, Yu. Valdau, E. Valetov, C. Weidemann, A. Wrońska, and P. Wüstner. Measurement of deuteron carbon vector analyzing powers in the kinetic energy range 170–380 mev. *The European Physical Journal A*, 56(8):211, Aug 2020. doi:10.1140/epja/s10050-020-00215-8.

[21] F. Müller, O. Javakhishvili, D. Shergelashvili, I. Keshelashvili, D. Mchedlishvili, F. Abusaif, A. Aggarwal, L. Barion, S. Basile, J. Böker, N. Canale, G. Ciullo, S. Dymov, O. Felden, M. Gagoshidze, R. Gebel, N. Demary, K. Grigoryev, D. Grzonka, T. Hahnraths, V. Hejny, A. Kacharava, V. Kamerdzhiev, S. Karanth, A. Kulikov, A. Lehrach, P. Lenisa, N. Lomidze, B. Lorentz, G. Macharashvili, A. Magiera, Z. Metreveli, A. Nass, N.N. Nikolaev, M. Nioradze, A. Pesce, V. Poncza, D. Prasuhn, J. Pretz, F. Rathmann, A. Saleev, T. Sefzick, Yu. Senichev, V. Shmakova, J. Slim, H. Soltner, E. Stephenson, H. Ströher, M. Tabidze, G. Tagliente, Yu. Uzikov, Yu. Valdau, T. Wagner, A. Wrońska, P. Wüstner, and M. Zurek. A new beam polarimeter at cosy to search for electric dipole moments of charged particles. *Journal of Instrumentation*, 15(12):P12005, dec 2020. doi:10.1088/1748-0221/15/12/P12005.

[22] M. Tanaka, T. Yamagata, S. Nakayama, M. Inoue, Y. Sakuragi, M. Kamimura, K. Goto, K. Katori, M. Yanagi, and H. Ogata. Observation of vector analyzing power in elastic scattering of 150-MeV ^{6}li on ^{12}c. *Phys. Rev. C*, 36:2146–2149, 1987. doi:10.1103/PhysRevC.36.2146.

[23] A. Nadasen, J. Brusoe, J. Farhat, T. Stevens, J. Williams, L. Nieman, J. S. Winfield, R. E. Warner, F. D. Becchetti, J. W. Jänecke, T. Annakkage, J. Bajema, D. Roberts, and H. S. Govinden. Unique potentials for the elastic scattering of 350 MeV ^{7}Li from ^{12}C and ^{28}Si. *Phys. Rev. C*, 52:1894–1899, 1995. doi:10.1103/PhysRevC.52.1894.

[24] W. R. Lozowski, D. Steski, H. Huang, and C. Naylor. Carbon micro-ribbon and strip polarimeter targets for the AGS and RHIC. *Nucl. Instrum. Meth. A*, 594:332–341, 2008. URL: https://www.sciencedirect.com/science/article/abs/pii/S0168900208002933, doi:10.1016/j.nima.2008.06.027.

[25] F. Rathmann. Estimating residual gas beam loss in the BNL AGS Booster: Model, numerical tools, and implications for a polarimeter chamber. Technical Report BNL-229699-2026-TECH, CA/AP/746, Brookhaven National Laboratory, April 2026. URL: https://technotes.bnl.gov/PDF?publicationId=229699.

[26] D. B. Steski, L. Sukhanova, A. Zelenski, and W. B. Christie. Recent developments in the production of carbon micro-ribbons for CNI polarimeters at BNL. *J. Radioanal. Nucl. Chem.*, 299(2):1035–1039, 2014. doi:10.1007/s10967-013-2646-0.

[27] D. Steski. RHIC and AGS CNI carbon target parameters, 2026. Private communication.

[28] W. M. Haynes, editor. *CRC Handbook of Chemistry and Physics*. CRC Press, Boca Raton, FL, 95th edition, 2014.

[29] K. Hock. Polarized ^{3}He in the Booster and AGS, 2025. Talk presented at BNL.

[30] Configuration manual: Polarized proton collider at RHIC. Technical Report C-A/AP/#455, Brookhaven National Laboratory, 2012. URL: https://www.agsrhichome.bnl.gov/AP/ap_notes/ap_note_455.pdf.

[31] Y. I. Makdisi. Measuring the proton beam polarization. In *Proc. Beam Instrumentation Workshop (BIW 1998)*, 1998. https://www.slac.stanford.edu/pubs/confproc/biw98/makdisi.pdf.

[32] F. Ajzenberg-Selove. Energy levels of light nuclei $a = 11$–12. *Nuclear Physics A*, 506:1–158, 1990. doi:10.1016/0375-9474(90)90271-M.

[33] T. Poikela et al. Timepix3: a 65k channel hybrid pixel readout chip with simultaneous ToA/ToT and sparse readout. *JINST*, 9:C05013, 2014. doi:10.1088/1748-0221/9/05/C05013.

[34] Hans-Jochen Trost, Peter Lezoch, and Udo Strohbusch. Simple optical model treatment of the elastic 3 He scattering. *Nucl. Phys. A*, 462:333–357, 1987. doi:10.1016/0375-9474(87)90551-3.

[35] D. Y. Pang, W. M. Dean, and A. M. Mukhamedzhanov. Optical model potential of $a = 3$ projectiles for 1p-shell nuclei. *Phys. Rev. C*, 91:024611, 2015. URL: https://link.aps.org/doi/10.1103/PhysRevC.91.024611.

[36] P. E. Hodgson. *The Optical Model of Elastic Scattering*. Oxford University Press, Oxford, 1963.

[37] G. R. Satchler. *Direct Nuclear Reactions*. Oxford University Press, Oxford, 1983.

[38] G. G. Ohlsen. Polarization transfer and spin correlation experiments in nuclear physics. *Reports on Progress in Physics*, 35(2):717–801, 1972. doi:10.1088/0034-4885/35/2/305.

[39] R. E. Pollock, W. A. Dezarn, M. Dzemidzic, J. Doskow, J. G. Hardie, H. O. Meyer, B. v. Przewoski, T. Rinckel, F. Sperisen, W. Haeberli, B. Lorentz, F. Rathmann, T. Wise, and P. V. Pancella. Calibration of the polarization of a beam of arbitrary energy in a storage ring. *Phys. Rev. E*, 55:7606–7611, Jun 1997. URL: https://link.aps.org/doi/10.1103/PhysRevE.55.7606, doi:10.1103/PhysRevE.55.7606.

[40] B. von Przewoski, F. Rathmann, W. A. Dezarn, J. Doskow, M. Dzemidzic, W. Haeberli, J. G. Hardie, B. Lorentz, H. O. Meyer, P. V. Pancella, R. E. Pollock, T. Rinckel, F. Sperisen, and T. Wise. Proton-proton analyzing power and spin correlation measurements between 250 and 450 MeV with an internal target in a storage ring. *Phys. Rev. C*, 58:1897, 1998. https://doi.org/10.1103/PhysRevC.58.1897. doi:10.1103/PhysRevC.58.1897.